Chapter 11
Miscellaneous Topics

11.1 Hypersonic Flows

In the advent of the space exploitation, the shock tube supported the atmospheric re-entry of space vehicles. Hence the space technology owed its success immensely to the shock wave research. Initially the design of the heat shield of re-entry vehicles became a main topic in the shock wave research but later it was shifted to hypersonic propulsions of SCRAM jet engines.

In the 1990s, a free piston shock tunnel was constructed in the Shock Wave Research Center of the Institute of Fluid Science in house. Figure 11.1 shows a sketch of the free piston shock tunnel. Hypersonic flow experiments were carried out under the collaboration with the National Aerospace Laboratory, Kakuda Branch. This shock tunnel was a pilot facility aiming to construct the high enthalpy shock tunnel (HEIEST) in the NAL Kakuda Branch in the near future. This free piston shock tunnel achieved the stagnation enthalpy of 4.8 MJ/kg producing the nozzle flow speed u_∞ of 2750 m/s, the stagnation temperature T_∞ of 387 K, the stagnation pressure p_∞ of 2.26 kPa, the stagnation density of ρ_∞ 2×10^{-2} kg/m^3, and resulting flow Mach number M_∞ of 6.99. A relatively uniform hypersonic nozzle flow was sustained for approximately 300 μs. Koremoto (2000) investigated the starting process of the nozzle flows. Hashimoto (2003) visualized flows over double wedges and double cones installed in the nozzle flow by shadowgraph and recorded in a high-speed video camera Shimadzu SH100.

11.1.1 Flows Over Double Wedges and Double Cones

Figure 11.2a, b show a double wedge model and a double cone model installed in the test section, respectively. The first wedge angle and the first half cone angle were 25° and the second wedge angles were varied to be θ = 40, 50, and 68° and

K. Takayama, *Visualization of Shock Wave Phenomena*,
https://doi.org/10.1007/978-3-030-19451-2_11

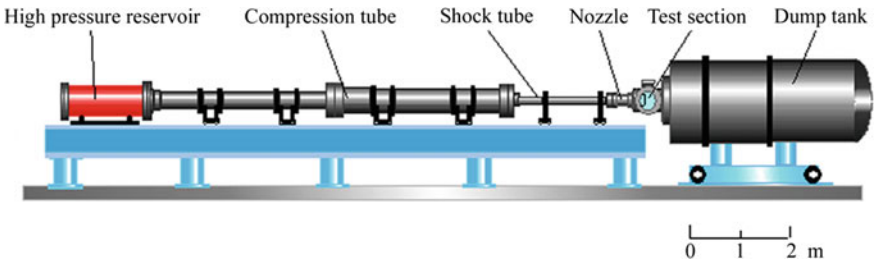

Fig. 11.1 The free piston shock tunnel of the SWRC, Tohoku University

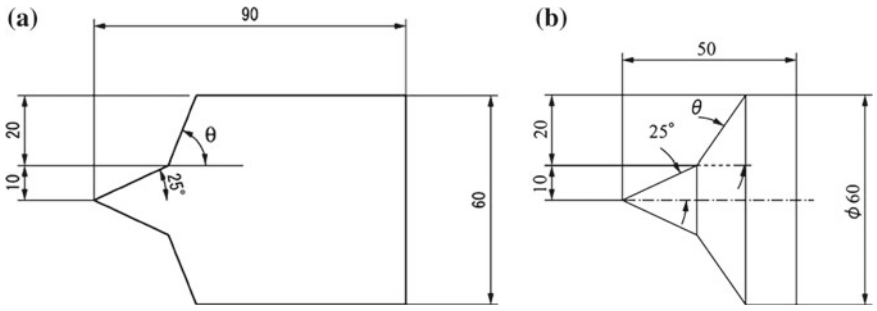

Fig. 11.2 Test models: **a** double wedge θ = 40, 50, 68°; **b** double cone θ = 40, 65°

second cone angles were varied to be θ = 40 and 65° as shown in Fig. 11.2. The double wedge model was 90 mm long and 60 mm diameter. The double cone model was 50 mm long and 60 mm diameter. Both of them were made of brass.

Figure 11.3a, c show images of direct shadowgraphs of the hypersonic flow over a double wedge of 25/50° and a double wedge of 25/68° double wedges, respectively, recorded by a high speed digital camera Shimadzu SH100 at the framing rate of 10^6 frame/s. A shock wave was attached at the leading edge of the first wedge. A detached shock appeared at the corner of the first and the second wedge. The boundary layer developed along the first wedge surface and separated ahead of the corner of the first and second wedges. A separation zone appeared at the corner, forming a recirculation region. However, it is not easy to identify flow features in recirculation regions over the double wedges and double cones by observing the framing pictures. To precisely interpret flow features, it was decided to make the flaming pictures rearrange in a streak display.

0.5 mm wide slices of the individual framing pictures were made along the double wedge surface or the double cone surface seen in Figs. 11.3a, c and 11.4a, c. The slices of sequential images were arranged in a sequential order, which eventually formed a streak picture. Figures 11.3b, d and 11.4b, d show resulting streak

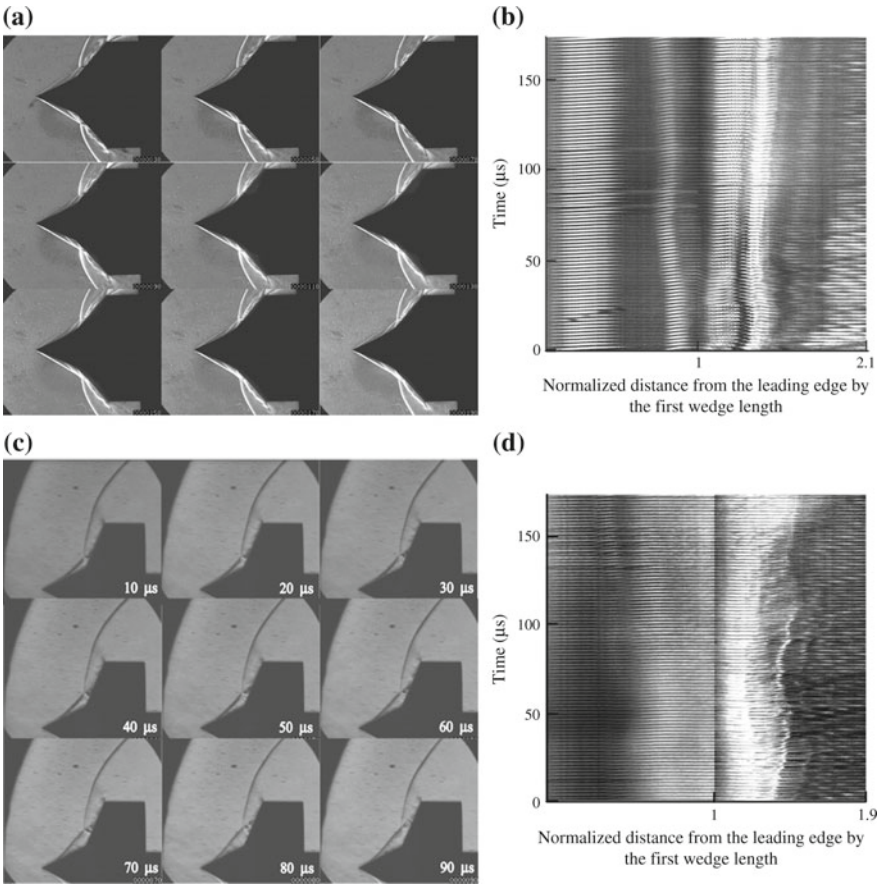

Fig. 11.3 High-speed video images of a hypersonic flow over double wedges: **a** direct shadow images over a 25/50° wedge; **b** streak display of (**a**); **c** direct shadow images over a 25/68° wedge; **d** streak display of (**c**) (Hashimoto 2003)

displays corresponding to Figs. 11.3a, c and 11.4a, c. The ordinate denotes elapsed time in μs and the abscissa denotes the distance normalized by the distance from the leading edge to the corner.

Figure 11.4a–d show hypersonic flows over double cones and direct shadow images and their streak displays are presented. The streak display indicates that the recirculation region fluctuates at higher frequency over the 25/65° double cone than over the 25/50° double cone. A similar trend is observed over the double wedges. This explains the usefulness of the streak display out of the high speed framing images.

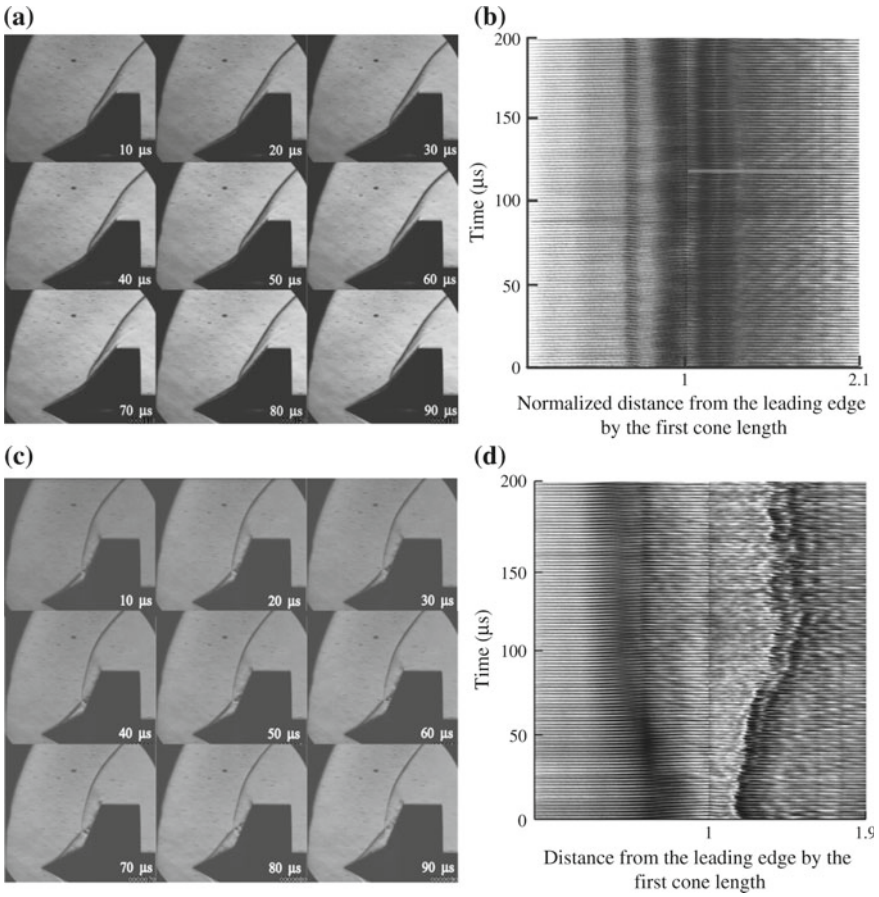

Fig. 11.4 High-speed video images of a hypersonic flow over double cones of 25/50° at 2.3 kPa, 390 K flow velocity of 2759 m/s: **a** direct shadow images over a 25/50° cone; **b** streak display of (**a**); **c** direct shadow images over a 25/65° cone; **d** streak display of (**c**) (Hashimoto 2003)

11.2 Ballistic Ranges

In the late 1980, a single stage powder gun was constructed and flights of projectiles were visualized. Projectiles' motions were measured with a VISAR (velocity interferometry from surface of any reflectors) and compared by an appropriate numerically simulation. The numerical code for simulating a two-stage light gas gun was based on the Random Choice Method and developed by Professor Gottlieb of the UTIAS. Figure 11.5 shows a two-stage light gas gun installed in the Shock Wave Research Center (Matsumura et al. 1990).

Smoke-less powder weighing 150 g was filled in a propellant chamber. A 60 mm diameter poly-carbonate piston weighing from 0.5 to 2.0 kg was placed

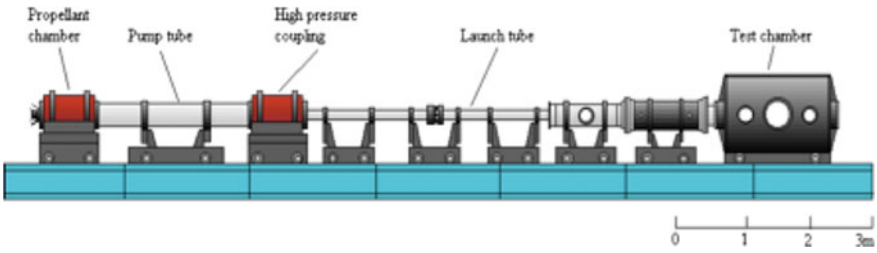

Fig. 11.5 Two-stage light gas gun (Matsumura et al. 1990)

in a 60 mm diameter and 3 m long pump tube. Helium at initial pressure of 0.5 MPa was filled in the pump tube. The heavy piston was accelerated by high pressures generated by controlled combustion of the smoke-less powder eventually compressed helium filled in high-pressure coupling up to 0.5 GPa elevating the temperature up to a few thousand K. The inertia mass of the high pressure coupling absorbed the high stress wave impulsively generated upon the impact of the heavy piston and maintained the high pressure and high temperature helium for a very short time. Then, a 14 mm diameter nylon projectile was accelerated along the acceleration tube and readily reached to maximum speed of 5 km/s.

11.2.1 Bow Shock in Front of Free Flight Blunt Bodies in Air

Figure 11.6 show bow shock waves appearing ahead of a free flight of blunt cylinder. Figure 11.6d–f are reconstructed three-dimensional holograms. Figure 11.6d was taken immediately after the projectile entering into the test chamber. The hologram was taken at the moment when the blunt cylinder just took over the precursory shock wave. The inclination angle θ of individual bow shock wave indicated the flight speed, that is $\sin\theta = a/u$, where a and u are the sound speed in air and the free flight speed, respectively.

In hot hypersonic experiments, a reliable data acquisition is one of the important tasks. Professor Park of NASA Ames advised that the shock stand-off distance over spheres demonstrated real gas effects, because the shock stand-off distances in an intermediate hypersonic flow region is sharply affected by the real gas effects. Shock stand-off distances in front of free flight spheres intermediate hypersonic flow region were visualized in the two-stage light gas gun (Nonaka 2000) and also in the free piston shock tunnel (Hashimoto 2003). Figure 11.7 summarizes previous experiments conducted in the Shock Wave Research Center. ρR is a hypersonic similarity parameter. The ordinate denotes dimension-less shock stand-off distance. The abscissa denotes the free flight speed in km/s. Red, olive color, light blue, and dark blue filled circles denote results of ballistic range experiments corresponding

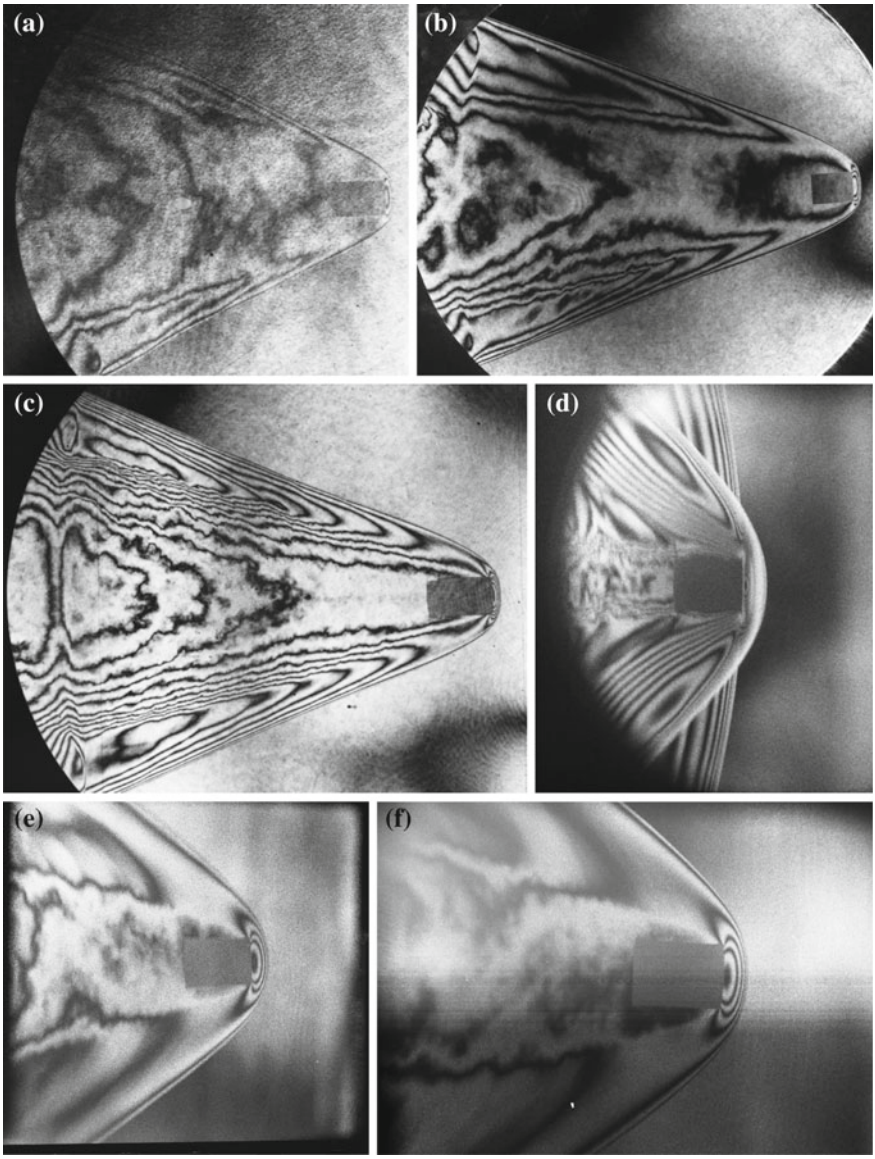

Fig. 11.6 Free flight of 10 mm diameter polycarbonate projectiles launched from a two-stage light gas gun: **a** #92101304, Ms = 2.56; **b** #92101601, Ms = 2.50; **c** #93022101, Ms = 2.77; **d** #98102901, Ms = 1.41, at 1013 hPa, 3-D hologram; **e** #98102902, Ms = 1.56, 3-D hologram; **f** #98102903, Ms = 1.49, 3-D hologram (Matsumura et al. 1990)

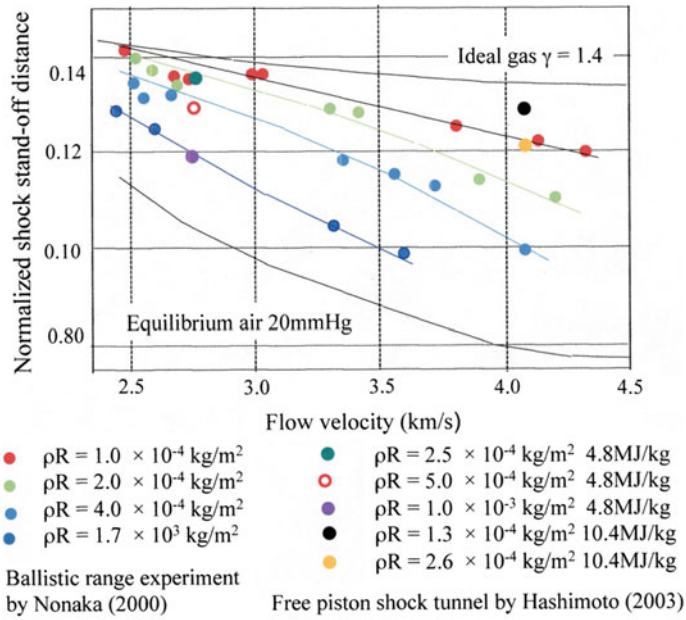

Fig. 11.7 Shock stand-off distance at intermediate hypersonic flow ranges collected by the ballistic range

to $\rho R = 1.7 \times 10^{-3}$ kg/m^2, $\rho R = 1.0 \times 10^{-4}$ kg/m^2, $\rho R = 2.0 \times 10^{-3}$ kg/m^2, $\rho R = 4.0 \times 10^{-4}$ kg/m^2 (Nonaka 2000), respectively, and black, red, and light blue open circles, a black filled circle, and a yellow filled circle denote result of free piston shock tunnel experiments corresponding to 2.5×10^{-4} kg/m^2, at 4.8 MJ/kg, 5.0×10^{-4} kg/m^2, at 4.8 MJ/kg, 1.0×10^{-3} kg/m^2, at 4.8 MJ/kg, 1.3×10^{-4} kg/m^2, at 10.4 MJ/kg, and 2.6×10^{-4} kg/m^2, at 10.4 MJ/kg (Hashimoto 2003), respectively. Experimental results corresponding to individual similarity parameters consistently lie on a line. The lines departed, depending on the values of similarity parameter, from the line of ideal gas having $\gamma = 1.4$ to the line estimated in the equilibrium air at 20 mmHg.

In 1998, a ballistic range was installed. Figure 11.8 shows an illustration of the SWRC ballistic range, which consists of a two-stage light gas gun and a 1.8 m diameter and 12 m long observation chamber. The two-stage light gas gun consists of a powder chamber, a high-pressure coupling, a 50 mm diameter and 3 m long pump tube, a launch tube, and a test chamber (Numata 2009). The launch tube is 3.4 m long and is convertible to either 15 or 50 mm diameter tube. The smokeless powder is installed in the powder chamber and is ignited following the US army standard. The high pressure coupling has a pre-stressed structure so that it has very compact if compare with the previous two-stage light gas gun. The observation chamber has a large space and hence various test sections can be accommodated.

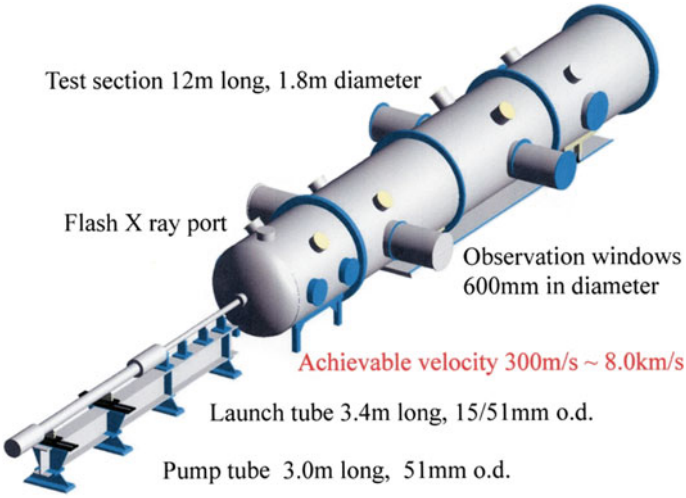

Fig. 11.8 SWRC ballistic range

Some test sections were filled not only with foreign gases but also with water. The observation chamber has two sets of pairs of 600 mm diameter optical windows and four sets of flash X-ray sources and detectors. Optical flow visualizations are conducted mostly by double exposure holographic interferometry and shadowgraph. For sequentially recording images, high speed camera ImaCon D-200 and Shimadzu digital high-speed camera SH100 were used. 15 mm diameter and 50 mm diameter projectiles are launched at speed ranging from the sonic speed to 8.0 km/s.

11.2.2 Free Flight in Combustible Mixtures

In order to visualize detonation waves induced by a high speed projectile, a compact test chamber filled with oxyhydrogen mixture was installed in the observation chamber. A 40 mm diameter nylon sphere was launched at 2.2 km/s into stoichiometric oxygen and hydrogen mixture $2H_2/O_2$ at 333 hPa/167 hPa. The experimental arrangement for launching a 40 mm diameter sphere into the test section was already explained in Fig. 4.23.

Figure 11.9a shows a detonation wave over a 40 mm sphere in fuel rich mixture ($2H_2$: 360 hPa, O2: 140 hPa). Figure 11.9b shows a detonation wave in stoichiometric mixture ($2H_2$: 333 hPa, O_2:167 hPa) at 2.2 km/s. In Fig. 11.9a, b, these interferograms comprised three interferograms taken at slightly different delay time. Figure 11.9c, d were enlargements of the shock layers corresponding to the images shown in Fig. 11.9a, b, respectively. It should be noticed that a slight deviation of shock stand-off distance was observed which were caused due to the slight

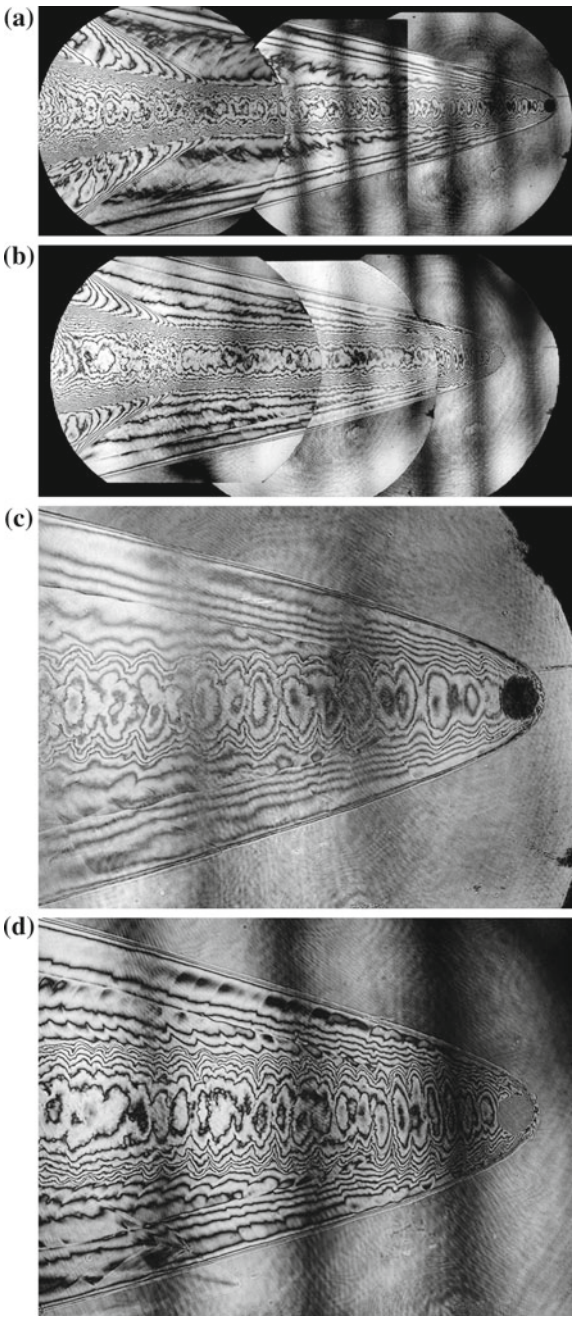

Fig. 11.9 Free flight in a combustible mixture: **a**, **c** projectile speed of 2.2 km/s in $2H_2$ = 360 hPa/ O_2 = 140 hPa, fuel rich mixture; **b**, **d** projectile speed of 2.2 km/s in $2H_2$ = 333 hPa/ O_2 = 167 hPa, stoichiometric mixture

difference in the constituents in combustible gas mixtures. The wakes have a coherent structure but its cycles are slightly different depending on the constituent of the combustible gas mixtures.

11.2.3 Space Debris Bumper Shields

Basic experiments of space debris bumper shields were conducted installing a test section in the observation chamber. A 15 mm launch tube was used projecting a 10 mm diameter stainless steel bearing ball. Figure 11.10 show sequential observation of shadow pictures recorded with a high speed video camera Shimadzu SP100 at framing rate of 10^6 frame/s and the exposure time of 125 ns. The pictures were displayed at every 24 μs interval. The target plate was aluminum alloy. In Fig. 11.10c, an impact flash was emitted and sustained for about 75 μs. The hypervelocity impact created stress waves in the targeting aluminum alloy. The stress created in the aluminum alloy well exceeded its yielding stress and hence the deformation in the aluminum alloy looked very much like that of liquid motion. Patterns of splashes observable on the target surface closely resembled in the splashes observed at high speed impact into a water surface.

Figure 11.11 show sequential observations of the penetration of a 10 mm diameter bearing ball at 2 km/s against a 10 mm thick composition of aluminum and Kevler. Images were recorded in the same way as described in Fig. 11.10. The target plate is the so-called stuffed bumper shield routinely used for the protection of the space structures from the debris attacks. The composite plate tested here are so designed as to stop the penetration of fragmented debris particles against the main shield.

11.2.4 Space Debris Bumper Shield at Cryogenic Temperature

The environmental temperature at which the satellites circulated varies widely from the cryogenic temperature about 100 K in the shadow of the earth to over 350 K at the sunny side. The bumper shield experiments are usually conducted at room temperature. Then the effect of the environmental temperature on high speed impact was investigated. At the cryogenic temperature, how can the high speed impact be affected? (Numata 2009).

Figure 11.12a shows a cryogenic test chamber and the installation of a frontal bumper made of aluminum alloy positioned at 100 mm separation distance from the main wall. Circulating liquid nitrogen, the temperature of the entire chamber and the test section were reached down to cryogenic temperature of 120 K was achieved. Figure 11.12a shows a frontal wall and main wall cooled by tightly contacting the supporting metal pieces as seen in Fig. 11.12b.

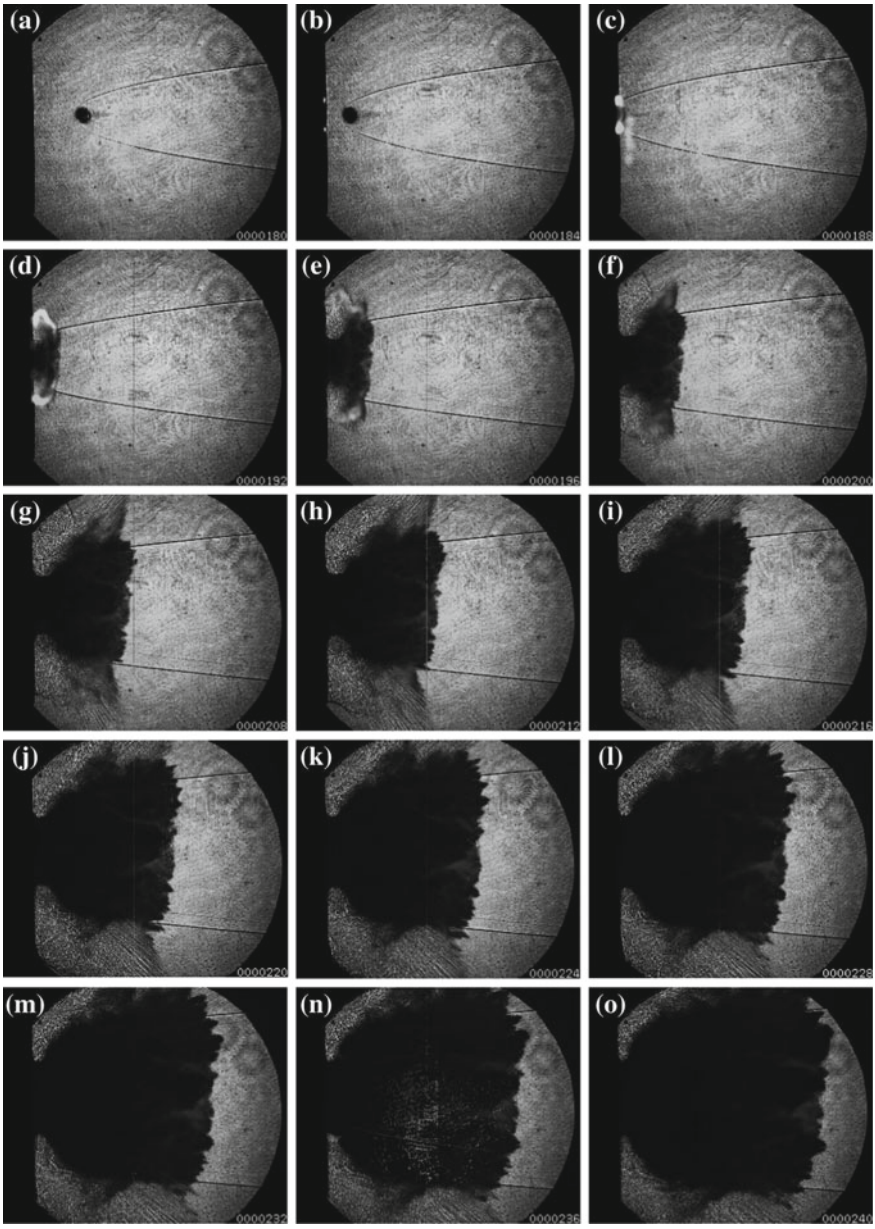

Fig. 11.10 Sequential observation of hypersonic impact of 10 mm diameter sphere against an aluminum bumper shield at entry speed of 3 km/s. Notice splash of impact fragments (Numata 2009)

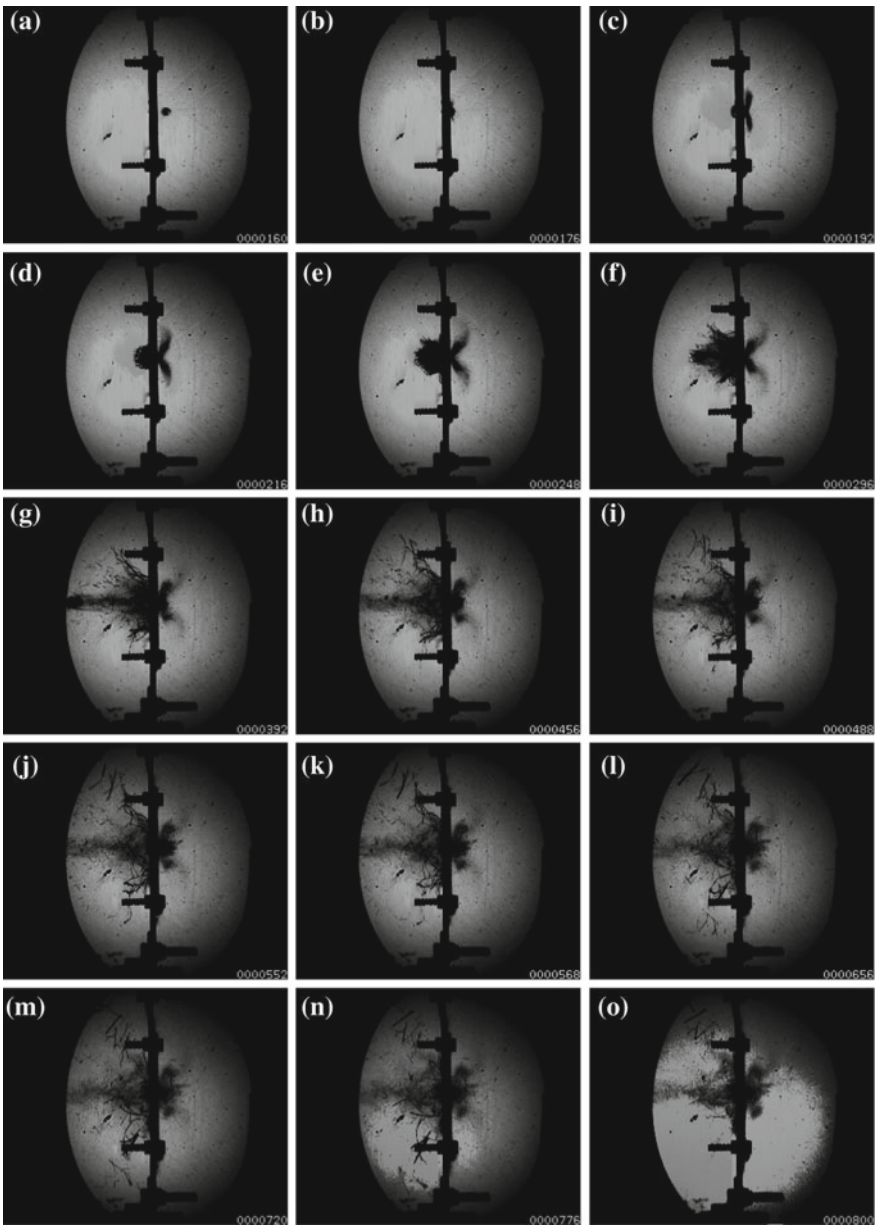

Fig. 11.11 Penetration of an aluminum/Kevler composite plate upon the impact of a projectile flying at 2 km/s (Numata 2009)

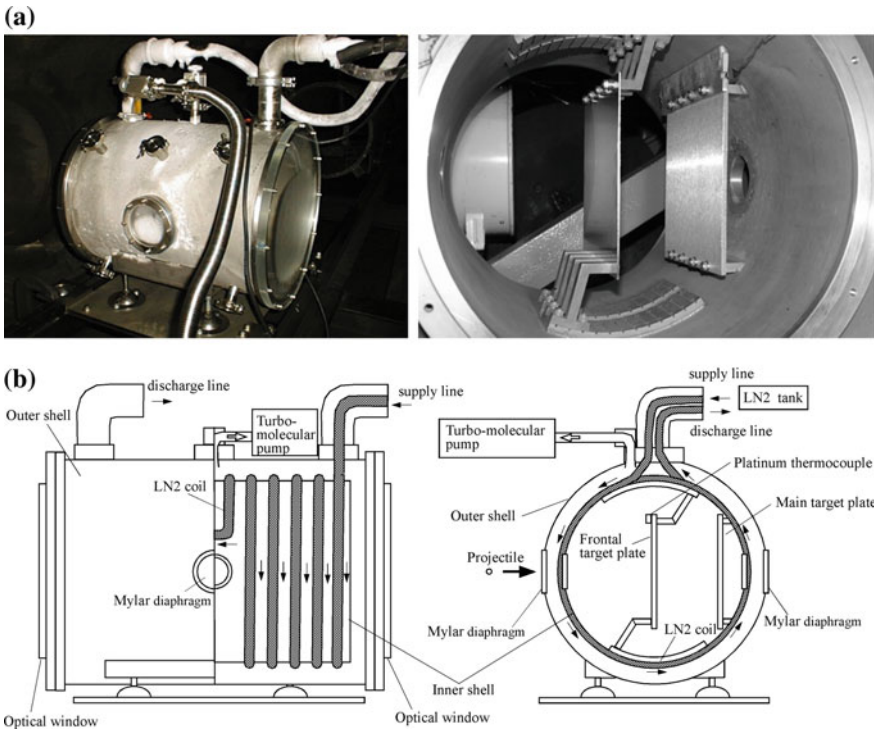

Fig. 11.12 Cryogenic test chamber: **a** test chamber; **b** internal structure of the test chamber (Numata 2009)

Figure 11.13a–c show images selected from high speed impact tests at projectile speeds of 2.7, 3.3, and 3.7 km/s against the wall at about 293 K, respectively. Figure 11.13d–f show images selected from high speed impact tests at projectile speeds at the impact speed of 2.8, 3.4, 3.7 km/s against the wall at about 118 K, respectively. The distributions of debris clouds did not differ significantly depending on the wall temperatures. However, the distribution of the debris clouds seemed to be more elongated at the impact speed 2.8 km/s, than that of 3.7 km/s.

It is concluded that the present analogue experiment revealed that the wall temperature did not affect significantly the debris cloud structure but it was strongly affected by the impact speed of the projectile.

Figure 11.14 show the result of an analogue experiment: the evolution of the debris cloud when a projectile impacted at 3.7 km/s against a bumper shield at 120 K. The images were recorded by Shimadzu SH 100 at the framing rate of 10^6 frame/s. At first, high-speed impacts of small fragments on the cryogenic wall created points of impact flashes. Then the main part of the debris cloud impacted following the generation of the intense impact flash. The main structure of the debris cloud was reflected. However, the main debris clouds were reflected from the main wall made of composite materials but never penetrated the main wall at this speed range.

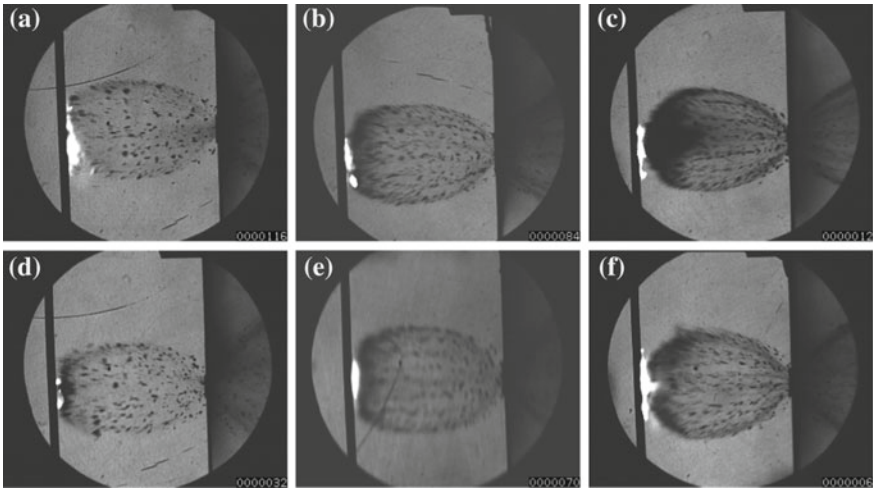

Fig. 11.13 Impacts on the main wall, comparison of wall temperatures: **a** projectile speed of 2.72 km/s and wall temperature at 295.2 K; **b** 3.33 km/s, 292.2 K; **c** 3.71 km/s, 294.2 K; **d** 2.78 km/s, 116.7 K; **e** 3.39 km/s, 118.8 K; **f** 3.70 km/s, 119.9 K (Numata 2009)

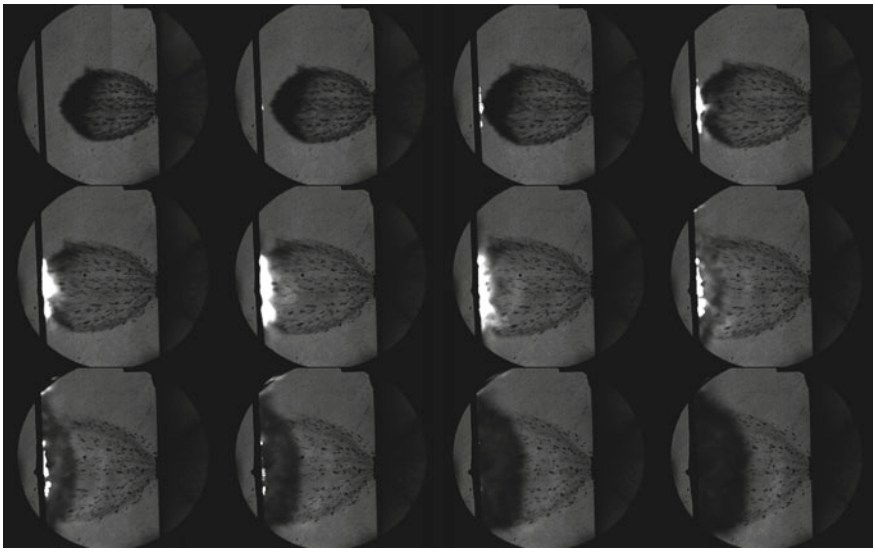

Fig. 11.14 The analogue experiment of space debris bumper shield at impact speed of 3.7 km/s against an aluminum plate at 120 K. Images were recorded by a high speed video camera Shimadzu SH100 (Numata 2009)

11.3 Shock Waves in Glass Plates

Shock waves were loaded onto glass plates by exploding AgN_3 pellets and resulting stress wave propagation in the glass plates were visualized using single and double exposure interferometry (Aratani 1998).

11.3.1 Shock Propagation in Tempered Glass Plates

A 10 mg AgN_3 pellet was placed at one of the focal points of an 8 mm thick and 106 mm × 150 mm elliptic tempered glass plate. The resulting high-pressures spontaneously generated a stress wave propagating inside the glass plate. Figure 11.15 show the evolution of stress wave propagation. Fringes represent density changes in the glass plates. At first, a hemi-spherical compression stress wave was generated at the center of the explosion and was reflected from the glass/air interface forming a spherical tensile stress wave. The spherical tensile stress wave was reflected from the other side of the glass plate forming a cylindrical tensile stress wave. Eventually the reflection of the spherical reflected tensile stress wave from another side of the glass plate formed a cylindrical compression stress wave. Trains of cylindrical tensile and compression stress waves propagating at the longitudinal speed were generated repeatedly as seen in Fig. 11.15b. The stress waves are reflected from its elliptic edge and eventually converged at the second focal point as seen in Fig. 11.15i. In Fig. 11.15b–e, transversal stress waves propagating behind the longitudinal stress wave and then cracked the focal area. It is noticed that cracks so far formed at first focal point have fine and course structures (Aratani 1998).

Figure 11.16 show an evolution of a compression stress wave propagating inside a glass plate. A 20 mg AgN_3 pellet was ignited placed at an edge of an 8 mm thick and 250 mm diameter tempered glass plate and spontaneously created circular compression stress waves as seen in Fig. 11.16a and the reflected tensile stress wave is about to focus in Fig. 11.16b.

A 10 mg AgN_3 pellet was attached on a side of a 10 mm thick and 150 mm 150 mm rectangular tempered glass plate and detonated forming trains of cylindrical tensile and compression stress waves as seen in Fig. 11.17. Figure 11.17 show sequentially the evolution of trains of these cylindrical stress waves propagation inside the rectangular glass plate and their reflection from the vertical side edges as seen in Fig. 11.17f–h. It should be noticed that the stress waves attenuate consistently with propagation, which shows a gradual decrease in the contrast of the intensity of the shadow as seen in Fig. 11.17i, j. The interactions of stress wavelets became very complex. The elapsed time is readily estimated from the distance the initial shock wave traveled on the upper side of the test piece.

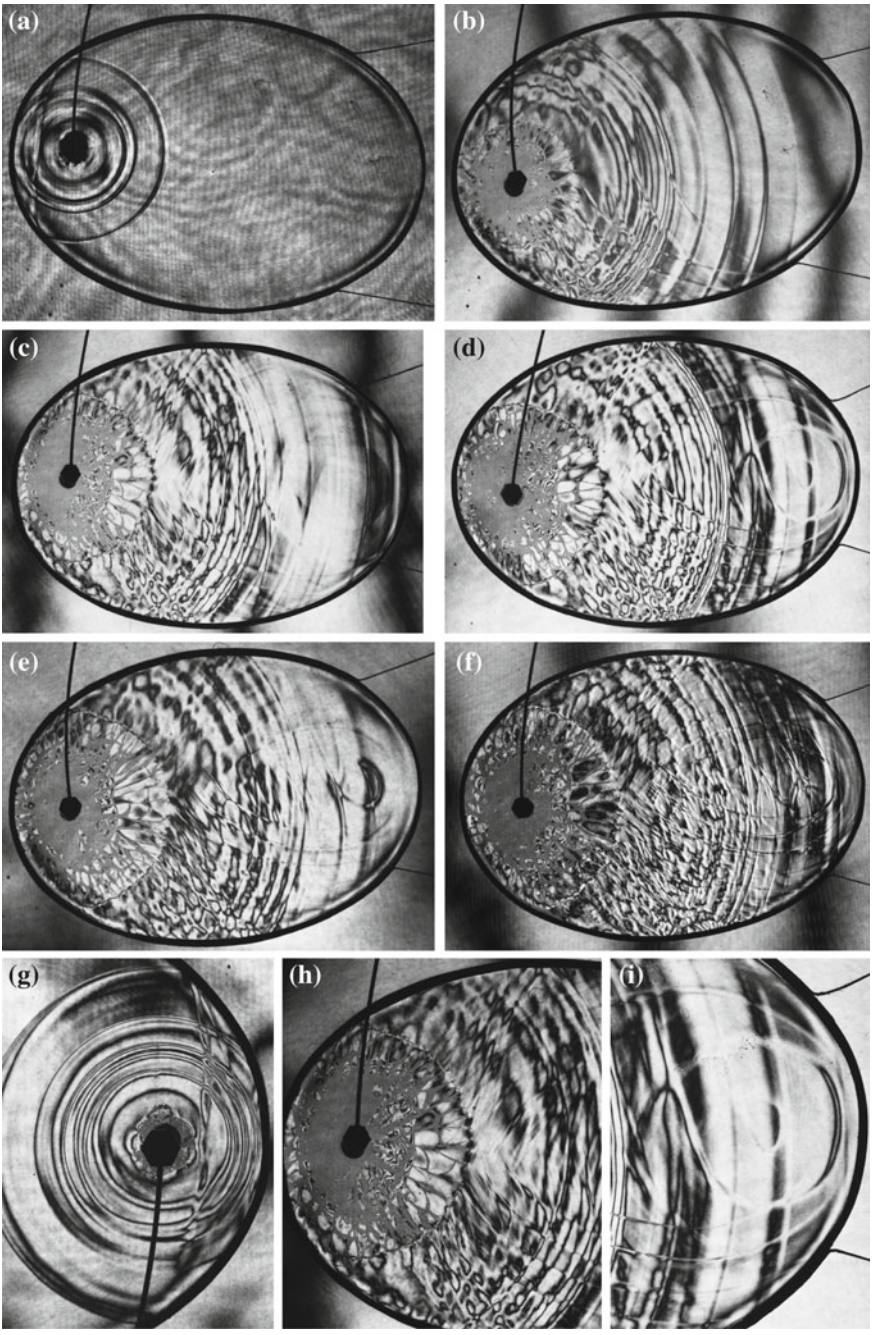

Fig. 11.15 Propagation of a stress wave created by a explosion of a 10 mg AgN_3 pellet on a 106 mm × 150 mm elliptic tempered 8.0 mm thick tempered glass plate: **a** #89012701, 125 μs from trigger point; **b** #89013006 137 μs; **c** #89013008, 143 μs; **d** #89013013, 145 μs; **e** #89013011, 146 μs; **f** #89013010, 147 μs; **g** #89013001, 127 μs; **h** #89013008 143 μs; **i** #89013013 145 μs (Aratani 1998)

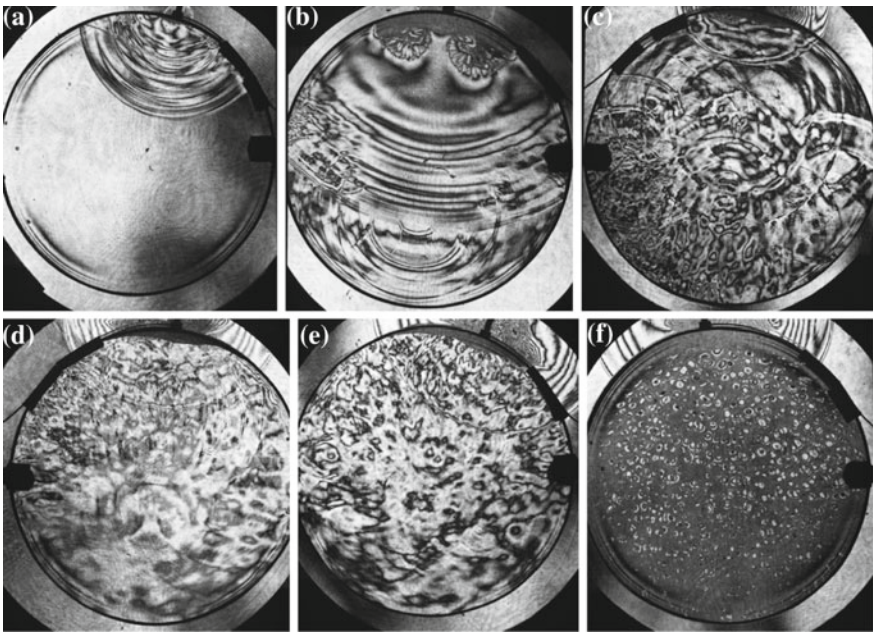

Fig. 11.16 Shock wave propagation over an 8 mm thick tempered glass plate. Shock wave is generated by exploding a 20 mg AgN_3 pellet at 291.0 K: **a** #87011404, 7 μs after ignition; **b** #87011603, 12 μs; **c** #87011407, 7 μs; **d** #87011604, 11 μs; **e** #87011406, 17 μs; **f** #87011606, 10 μs (Aratani 1998)

11.3.2 Laser Induced Shock Wave Propagation in Acrylic Blocks

A collimated Q-switched ruby laser beam was focused at 10 mm distance from the edge of a 50 mm × 90 mm × 150 mm acrylic plate as seen in Fig. 11.18a. When a Q-switched ruby laser having energy of 1 J/pulse and pulse width of 25 ns was focused in a point of about 0.1 mm in diameter, such an intense energy deposition in such a confined space instantaneously generates high temperatures and high pressures enough to vaporize the acryl and to create micro cracks which drive shock waves or compression waves even in acryl. However, the laser beam was not necessarily focused sharply at a point but the zone of focusing was slightly elongated to the direction of its irradiation. Hence the resulting cavity in the acryl was not a point but stretched cavity accompanying cracks over it. Trains of compression wavelets were generated from the cavities as seen in Fig. 11.18a. Figure 11.18c shows the double exposure interferogram of a cylindrical compression stress wave. Figure 11.18d shows a single exposure interferogram of the cylindrical shock wave. The laser beam was focused from a vertical direction and hence a vertically stretched cavity was observed.

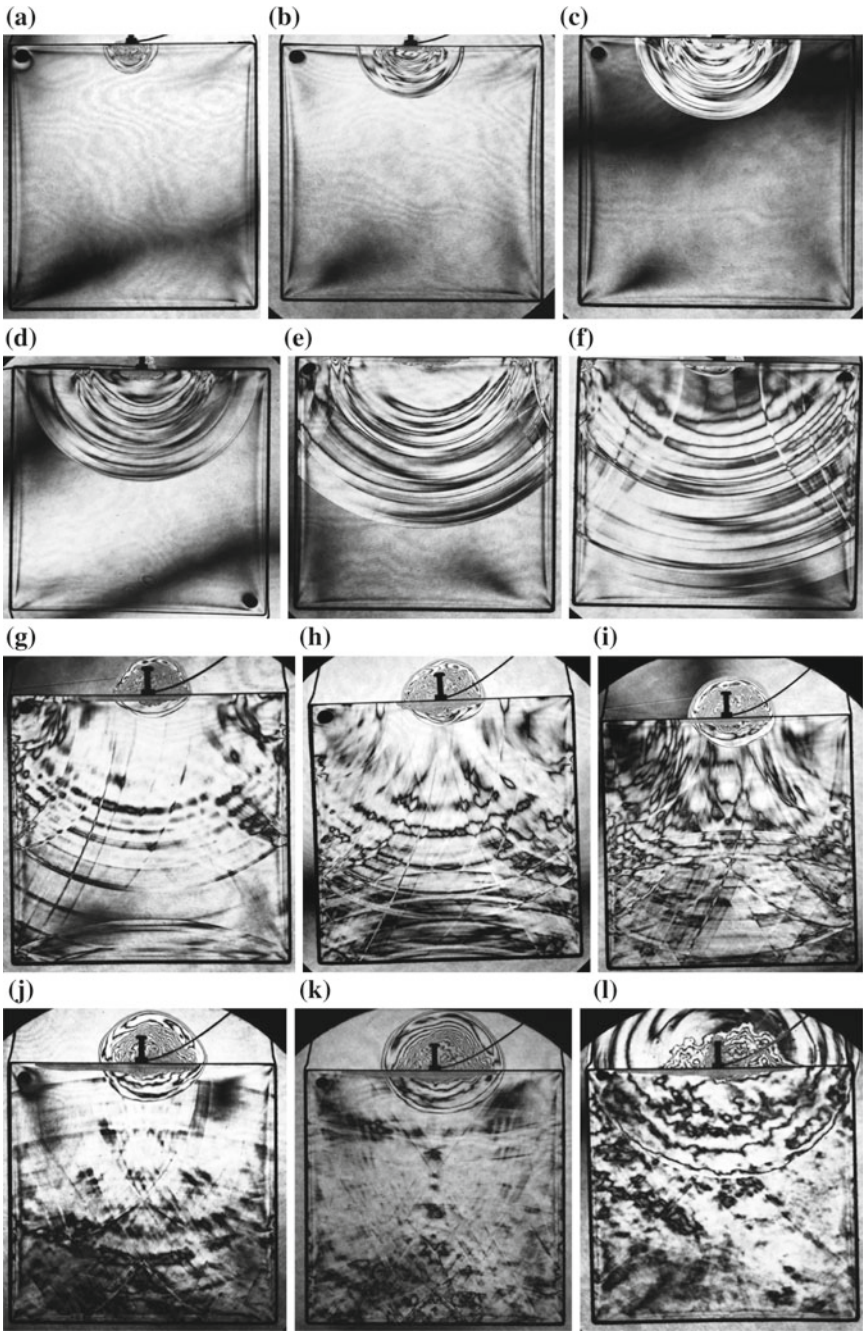

Fig. 11.17 Propagation of stress waves in a 150 mm × 150 mm and 10 mm in thickness rectangular #90082701; **b**#90082804; **c** #90082801; **d** #90082802; **e** #90082901; **f** #90082903; **g** #90082904; **h** #90083001; **i** #90083002; **j** #90083003; **k** #90083101; **l** #90083103 (Aratani 1998)

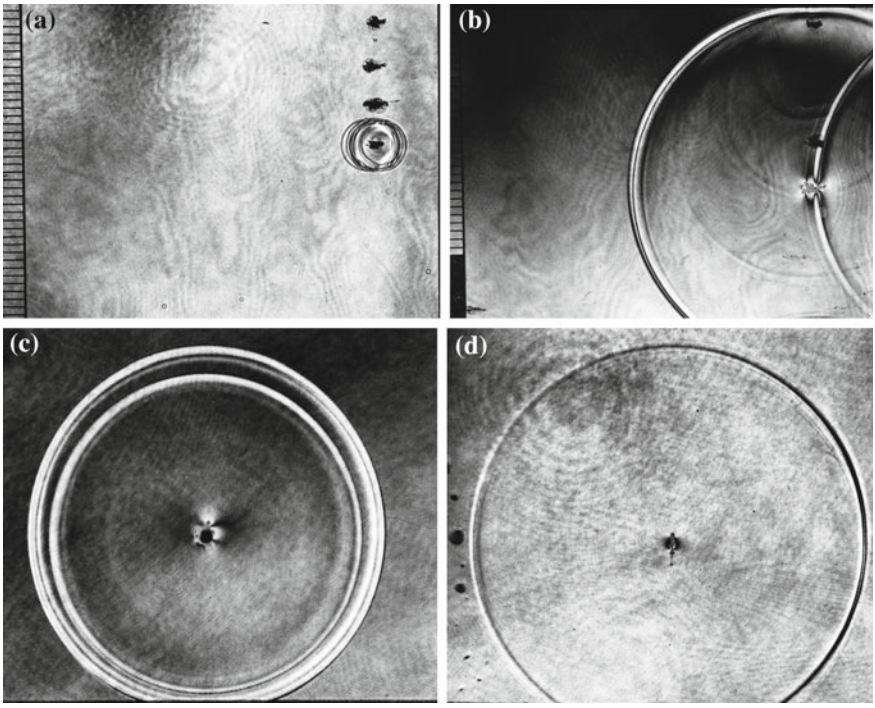

Fig. 11.18 Laser focusing induced stress waves. 1 J Q-switched ruby laser beam was focused in a 50 mm × 90 mm × 150 mm acrylic plate: **a** #85120206, laser bean was focused at 10 mm from the edge; **b** #85120210 at 8 μs from laser focusing; **c** #85120614; **d** #85111904

11.3.3 Shock Wave Propagation in Foam

Figure 11.19 shows a diaphragm-less shock tube consisting of a 230 mm diameter high pressure chamber, a co-axially arranged 60 mm × 150 mm low pressure channel, and about 1700 mm long test section. The structure of this diaphragm-less shock tube was already described by Yang (1995). The test section was specially modified to accommodate a 60 mm × 150 mm and 1200 mm long polyurethane foam, which was tightly inserted into the 1700 mm long test section as shown in Fig. 11.19 (Kitagawa et al. 2006).

Figure 11.20a shows a 60 mm × 150 mm polyurethane foam inserted in the 60 mm × 150 mm shock tube. In order to visualize the interaction of the foam with the reflected shock wave of Ms = 1.50 in the vicinity of the end wall of the 60 mm × 150 mm shock tube, a diffuse holographic interferometry was adopted. The single exposure collimated *OB* uniformly illuminated the foam's surface on which yellow fluorescent paint was sprayed. Then, the reflected *OB* from the deformed foam carried the holographic information of the deformed foam and was recorded on a holographic film. To ensure the deformation of the foam, 2 mm

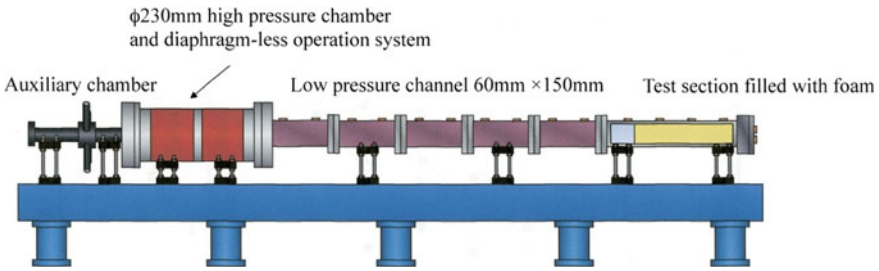

Fig. 11.19 A 60 mm × 150 mm diaphragm-less shock tube modified to perform shock wave propagation in polyurethane foam

diameter black dots were printed in a space of 5 mm × 5 mm on the foam surface as seen in Fig. 11.20a. Figure 11.20b shows the deformation of the foam interacted with the reflected shock wave. In the analytical model, the wave motion in the foam and its deformation should be one-dimensional. The predicted pressures and temperatures in the foam and in air in the vicinity of the end wall can reach much higher values than those predicted in a pure gas. Indeed in the shock tube having a polyurethane foam inserted at its end wall, the foam temperature at the end wall became so high that the foam indeed melted. This finding agreed well with the prediction.

In Fig. 11.20b the foam deformed two-dimensionally. The deformation pattern resembles very much like the bifurcation of a reflected shock wave occurring in the vicinity of the shock tube end wall in pure gas. In the case of a foam shock tube, the pressure behind the reflected shock wave became so high that the criteria proposed by Mark (1956) would be satisfied and hence an analogous pattern to the bifurcation would appear. If a two-dimensional analytical model of a foam shock tube may exist, it would be good to reproduce the pattern as shown in Fig. 11.20b.

11.3.4 Shock Waves in Sand Layers

It is appropriate to apply an established method of visualizing shock waves in gases to shock wave propagations in sand layers. Sand grains under study are standard Eglin sands. Figure 11.21 shows a microscopic view of the Eglin sand. Their diameter ranges from 330 to 500 μm (Yamamoto et al. 2015).

11.3.4.1 Point Explosion in a Sand Layer

At first a 10 mg AgN_3 pellet was exploded at the center a cylindrical chamber having 100 mm in diameter and 155 mm in height filled with Eglin sands. Eglin sand grains were poured into the test section and the bulk density was about

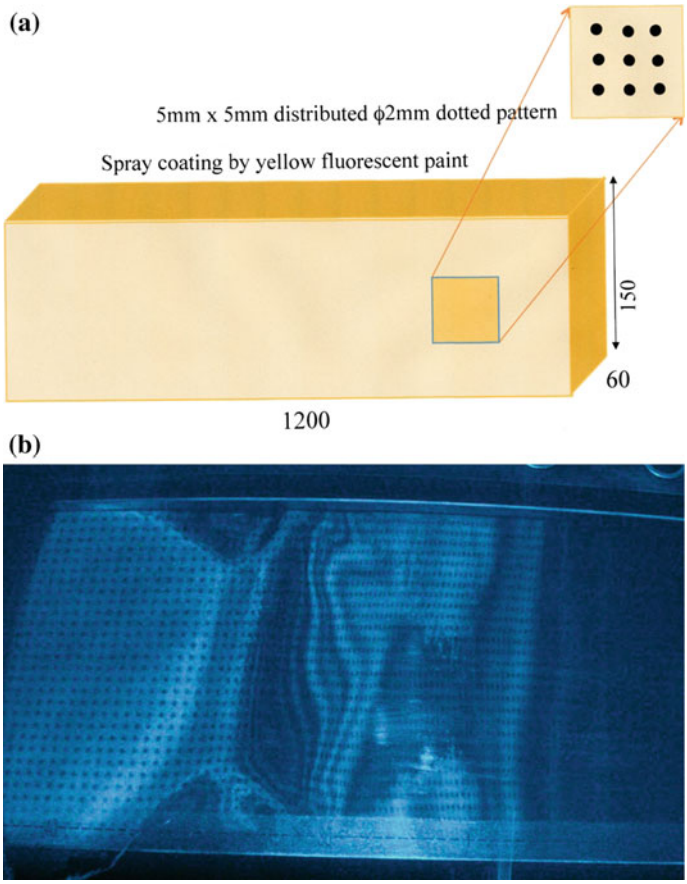

Fig. 11.20 Deformation of polyurethane foam upon shock wave loading: **a** foam model; **b** diffuse holographic observation (Kitagawa et al. 2006)

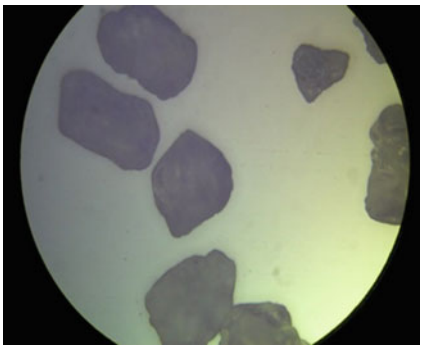

Fig. 11.21 Microscopic view of Eglin sand grains (Yamamoto et al. 2015)

Fig. 11.22 The cross sections of a point explosion in a sand layer filled with Eglin sands (Yamamoto et al. 2015)

1.55 g/cm^3. In order to quantitatively identify the deformations of the sands layer generated by a shock wave loading, thin layers of colored sand grains of the blue upper layer, black, brown, yellow, red, and the last brown layer are placed horizontally and in a nearly equal interval in the sand layer. The explosion at the center of the chamber spontaneously moved the sand layer, which eventually deformed the colored sand layers. As soon as the explosion was over and the movements of sand grains were ceased, the entire test piece was submerged into a liquid named Permeate™ (D&D Corp. Japan), which is volatile liquid and has a so low surface tension that it eventually permeated into the spaces among sand grains. When the liquid evaporated and the sand grains were tightly solidified, the frozen specimen was divided into two pieces.

Figure 11.22 shows the cross sections of the half-cut test piece. The sand grains were moved due to the exposure of high pressures at approximately several hundred MPa in the vicinity of the explosion center. The deformation of the color layers indicated the memory of motions of sand grains, in short, shattered by the spherical shock wave at first and by the reflected shock wave from the acrylic wall. The blue and black colored layers initially in the first and second layers from the upper surface were shattered upward and squeezed toward the side. The brown layer initially in the third layer was deformed upward but remained its closed shape. The sand grains located close to center of explosion changes were fragmented and became whitish. The color layers located below the position of the explosion center were not deformed significantly because the shock wave reflection from the bottom of the test chamber.

11.3.4.2 Penetration of High Speed Sphere into Sand Layers

Encouraged by the results of point explosions in a sand layer, the impingement of a high speed sphere vertically into a sand layer was investigated. A compact vertical powder gun was constructed as illustrated in Fig. 11.23. The basic part of this powder gun was once used to create the high-speed fuel jets experiment. Since this is a compact gun, preparatory experiments were carried out to control the delay time of the ignition smoke-less powder. Initially, a method of the laser ignition of a 10 mg AgN_3 pellet was adopted to ignite black powder and then to initiate the simultaneous combustion of the smoke-less powder. However, it was eventually revealed that the uncertainty existing in simultaneous combustion of the smokeless powder was uncontrollable. Then this compact gun followed the traditional method of impacting the primer with a mechanical impact. A primer containing smokeless powder (HS-7) weighing 3 g and a propellant comprising of black powder weighing 1.2 g started the ignition of smokeless powder (H50-BMG) weighing 5.0 g. The high-pressure so far created in a powder chamber drove a 9.5 mm diameter stainless steel bearing ball which was contained in a 14 mm diameter four-split sabot made of polycarbonate. The combination of the sabot and the bearing ball was accelerated through a vertical launch tube and propagated through a perforated tube. Compression waves and a resulting shock wave were expected to attenuate through the perforation. The sabot remover was placed at the end of the

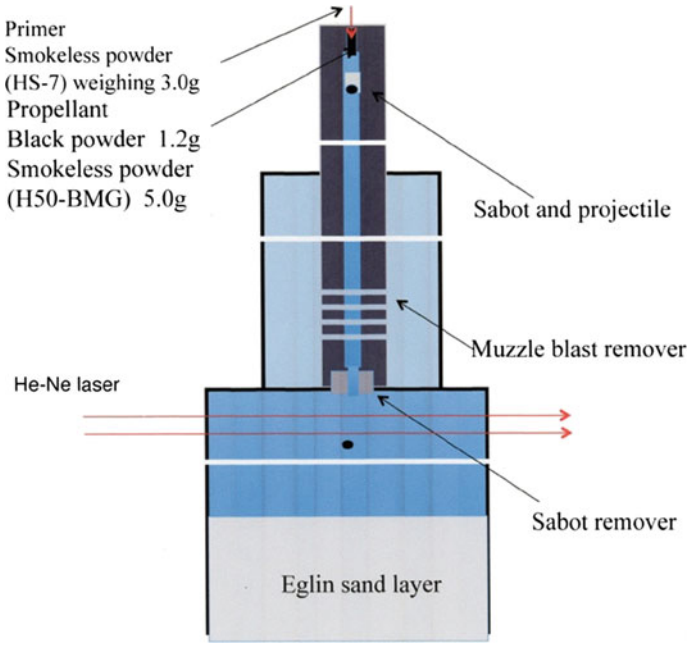

Fig. 11.23 Experimental setup of launching a 9.5 mm diameter sphere into a sand layer

perforation tube. Upon impacting on the sabot remover, only the bearing ball could pass through the sabot remover but the main part of the sabot squeezed into the edge of the sabot remover. The bearing ball speed was measured in the position located immediately after passing through the sabot remover or just before impacting the sand layer by measuring the time interval of the bearing ball intersecting the two He–Ne laser beams.

Figure 11.24 shows a rectangular cross sectional test section. This test section was designed to monitor the deformation of the sand layer occuring the penetration of 9.5 mm diameter bearing ball by distributing thin layers of colored sand grains horizontally embedded in the test section as illustrated. The test had a 33 mm 100 mm cross section and 250 mm in depth and comprised of a 25 mm thick frontal acrylic plate for the visualization, a 25 mm thick stain-less steel rear wall, and 50 mm wide and 50 mm thick brass side walls. A 9.5 mm diameter bearing ball made of stainless steel was projected vertically at 1.01 km/s as shown in Fig. 11.24 and its entry speed was measured in front the test section using the time of flight method. The test section was obliquely illuminated with a flood lamp and the variation of images monitored on the acrylic plate was recorded with a high speed digital camera Shimadzu SH100 with the framing rate of 10^6 frame/s and the exposure time of 125 ns. When the projectile propagated through the sand layer, a luminosity was emitted in the vicinity of the projectile. The luminosity was created by the disintegration quartz grains exposed to a shock wave.

0.2 mm diameter optical fibers transmitting a He–Ne laser beam were horizontally suspended and were distributed at given intervals along the center axis.

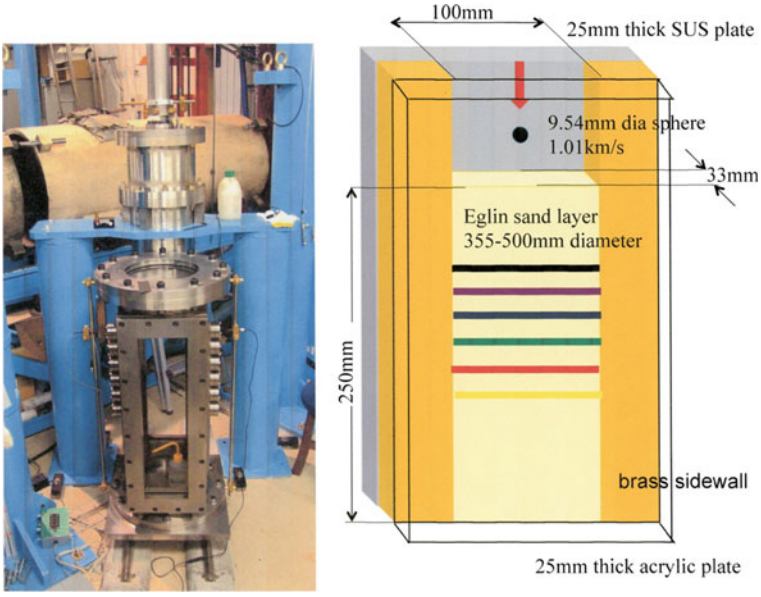

Fig. 11.24 The vertical two-stage gun and the illustration of the test section

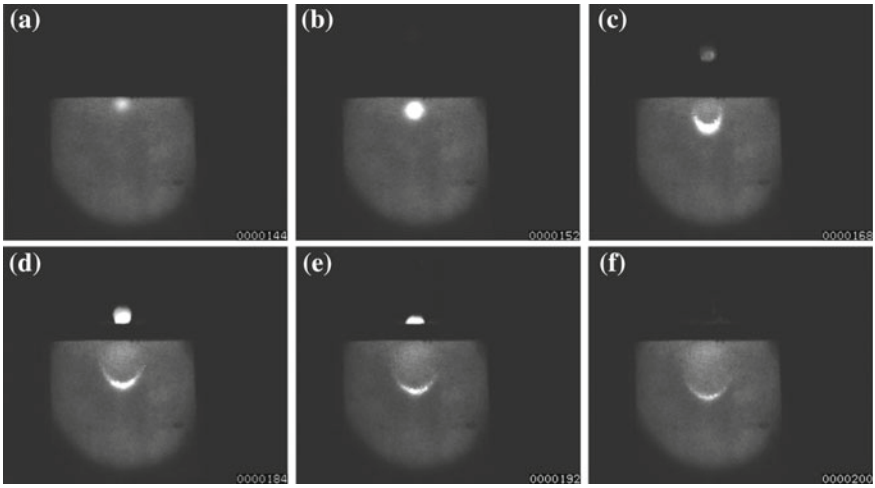

Fig. 11.25 The luminous emission at a projectile impact into sand layer: **a** 8 μs from entry; **b** 16 μs from entry; **c** 32 μs from entry; **d** 40 μs from entry; **e** 48 μs from entry; **f** 56 μs from entry (Yamamoto et al. 2015)

The on-off signals created at the moment when the projectile ruptured the optical fibers would provide the attenuation of the projectile through the sand layer. The measured projectile motion was compared with the result of visualization.

Figure 11.25 show the projectile movement observed at every 8 μs up to elapsed time of 56 μs from the impingement of the projectile on the sand layer. Figure 11.26 show the sequential observation up to 168 μs. Figure 11.25a shows the state at 8 μs from the impingement. A quartz crystal generates electric charges when exposed to high pressures or deformation. It is known that a quartz crystal emits a luminosity of wave length of 654 nm when cracked by an external force. This is the inherited character of a quartz crystal and the so-called piezo effect.

When the projectile entered into the sand layer, the surface of an impacted sand layer was shining faintly as seen in Fig. 11.25a. It should be noticed that as seen in Fig. 11.24, the sphere penetrated inside a 33 mm wide sand layer and the luminosity occurred about 10 mm away from the inner wall. When the sphere fully penetrated the sand layer, the surface of the entire sphere was exposed to significantly high shear stress so that the sand grains would emit intense luminosity. Then a circular luminous front was observed as seen in Fig. 11.25b.

The brightness of the luminosity is related to the degree of fragmentation of the sand grains. The finest size of corn starch powders was observed among the fractured sand grains attached to the sphere surface. The fragmented sand grains inside the shock layer which were located a few mm away from the sphere surface had sizes of sugar grains. In Fig. 11.25c, the shape of luminous front resembles a bow shock wave observed at 10 mm away from the side wall. With elapsing time, the radius of the detached bow shock wave gradually was enlarged and gradually

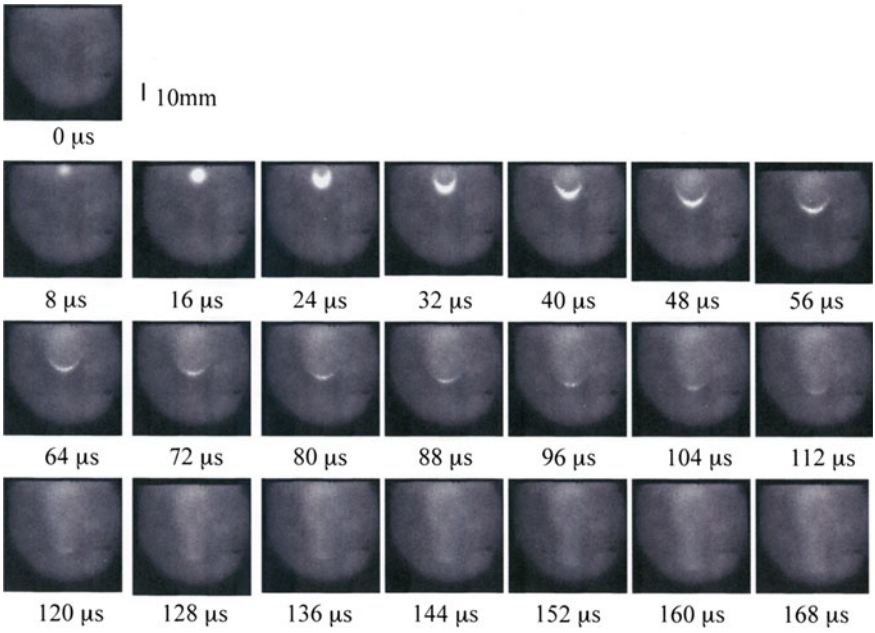

Fig. 11.26 Sequential observation of projectile penetration #13031102 (Yamamoto et al. 2015)

broadened. At the same time the luminous front became fainter. A faint front appearing above the sphere observed in Fig. 11.25c was caused by a remnant of the deformed sabot. The flood lamp illuminated the field of view not necessarily uniformly and then the sabot fragment looked faint as the edge of the flood lamp illuminated, whereas as seen in Fig. 11.25d the remnant of the sabot looked brighter as illuminated with central part of the flood lamp. It should be noticed that at 10 mm above the sand surface, the field of view was blocked. The bulk density of the sand layer is 1.55 g/cm^3. This value is significantly lower than that in air/sand mixtures tested in sand compaction experiments. In evaluating the time variation of luminous fronts, the sound speed in the sand layer was found about 180 m/s. This value is much slower than that in air.

Figure 11.26 show the sequential observation up to later time. The entry speed was 1.01 km/s which is equivalent to Ms = 5.5 based on the estimated sound speed in the present sand layer of 180 m/s. Therefore, the bow shock is detached closely when impacted the sand layer. If the shock wave is detached in a similar manner as it appears in air, the ratio of a shock stand-off distance δ to the sphere of diameter D, δ/D = 0.1 (Liepmann and Roshko 1960). Therefore, the shining bow shock waves are located very close to the sphere as seen in Fig. 11.26b at 16 μs. The sphere decelerated and the corresponding Ms quickly decreases to sonic speed. Then the shock stand-off distance is elongated quickly as already discussed in penetration of a supersonic sphere into water as shown in Fig. 9.69 in Chap. 9.

Figure 11.26c, d were taken at 24–32 μs from the projectile impact on the sand layer. The sphere is further decelerated and the radii of curvature of the detached shock wave increased. Eventually at 48 μs as seen in Fig. 11.26f, the detached shock wave would be repeatedly reflected from the sidewalls and eventually turned into a cylindrical shock wave. The central part of the luminous front is still faintly shining. Even though the speed of the detached shock wave approached gradually to the sonic speed, the luminosity started fading. At 168 μs, the sphere stopped completely. Measuring the distribution of the brightness along the center line, the trajectory of the sphere would be estimated. If analyzing the time variation of the trajectory of luminous front, the attenuation of the sphere and the transition of the bow shock wave to the sonic wave would be readily determined.

Figure 11.27 summarizes the variation of the brightness along the center line of the individual pictures shown in Fig. 11.26. The ordinate denotes the degree of brightness in the individual frames in arbitrary unit. The abscissa denotes the distance in pixels. The origin corresponds to the sand layer surface. The number on the

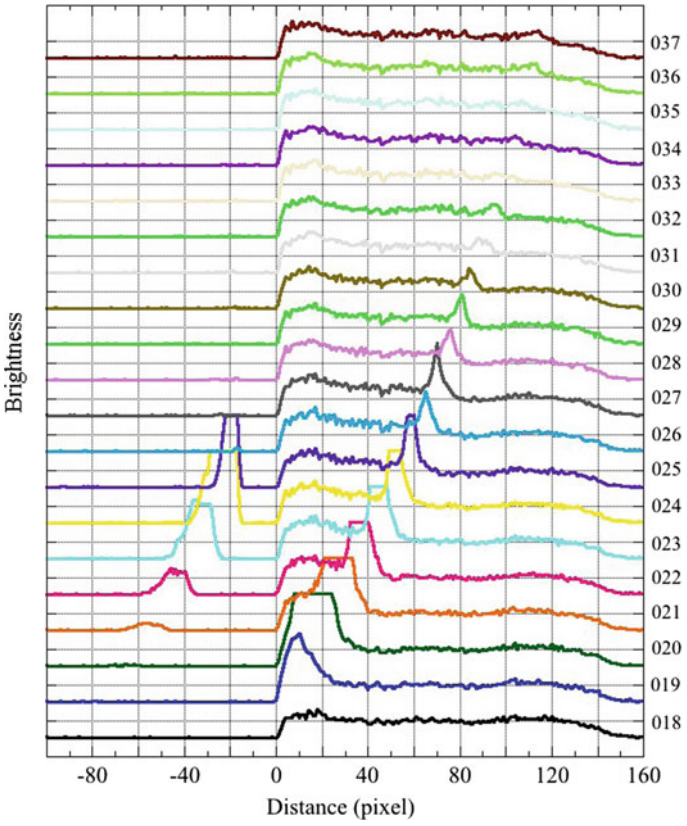

Fig. 11.27 The time variation of the luminous front profile, summary of Fig. 11.26

right shows frame number. The ordinate denotes the elapsed time every 8 μs interval. The intensity profile of the frame #18 corresponds to Fig. 11.26a at 0 μs. The intensity profile of the frame No. 037 corresponds to elapsed time of 168 μs. The luminosity sharply increases from #20 to #22 and the maximal luminosity appears at the frame #20 or 16 μs. and the peak brightness gradually decreases. The luminous front started widening and stretching from #26 to #37, indicating the increase of the shock stand-off distance of the bow shock. Tracing the trajectory of luminous front, the trajectory of bow shock wave can be estimated. Then the resulting speed of luminous front is about 150–200 m/s. This value is almost in the range of the sound speed in the sand layer. It is noticed that from the #36 to #37 at 160–168 μs, the projectile moved very slowly but the luminous front was still resolved.

In conclusion, a method routinely used in the shock wave research was successfully applied to the diagnostics of sand dynamics. The observation of luminous emissions appearing in shock layer is found a useful method. Improving the present experimental arrangement, the reflection of bow shock wave from the solid boundary may have been observable. The critical transition of reflected shock waves in sand layers will have been measured from these compact experiments.

Immediately after the impact experiment, test pieces were carefully immersed deeply in a chamber filled with the Permeate™ (D&D Corp. Japan). The specimens were divided into two segments. Then, structures of specimens were found well preserved the projectile motion. Figure 11.28a, b show the left and the right sides of specimen of a 100 mm diameter × 120 mm long cylindrical sand layer impacted at speed of 1.6 km/s. The surface of the sand layer was inclined by 30°, then the sphere impacted obliquely and propagated toward the shallower side. Initially horizontally distributed color layers were deformed indicating the sphere's oblique movement by observing the pattern of dragging the color layers.

White sand grains were observed along the sphere's trajectory. The white sand powders adhered to the sphere's surface were caused due to the presence of a very high shear force and high temperature at the sphere surface. During sand grains' fragmentations, the quart grains emitted luminosity forming a shining circular area. The white powders filling the space between stretched blue color layers and crashed sand grains would definitely emit the intense luminosity during the sphere's high-speed penetration. The sphere was probably spinning and then ground the sand grains into powders. Due to the spinning motion, the sphere bounced from the bottom of the sand layer and stopped. It should be noticed that during the early experiments the sabot was successfully plugged at the entrance of the sabot remover and only the sphere impinged the sand layer. Then the thermal decomposition never happened to occur. This is the reason why fragmented sand grains remained fresh white powder as seen in Fig. 11.28a, b.

Figure 11.28c shows the penetration onto a 30° tilted 100 mm diameter × 120 mm long cylindrical sand layer surface at the penetration speed of 1.01 k/s. Only the first black color layer was significantly deformed, unlike observation in Fig. 11.28a, b, the other color layers deformed symmetrically. At the penetration depth of 80 mm, the sphere stopped but slightly reflected obliquely

Fig. 11.28 Penetration of sphere into sand layers: **a**, **b** impact against oblique surface at 1.93 km/s: **c** #11030201, 1.02 km/s; **d** #13032901, 1.01 km/s; **e** enlargement of (**d**) (Yamamoto et al. 2015)

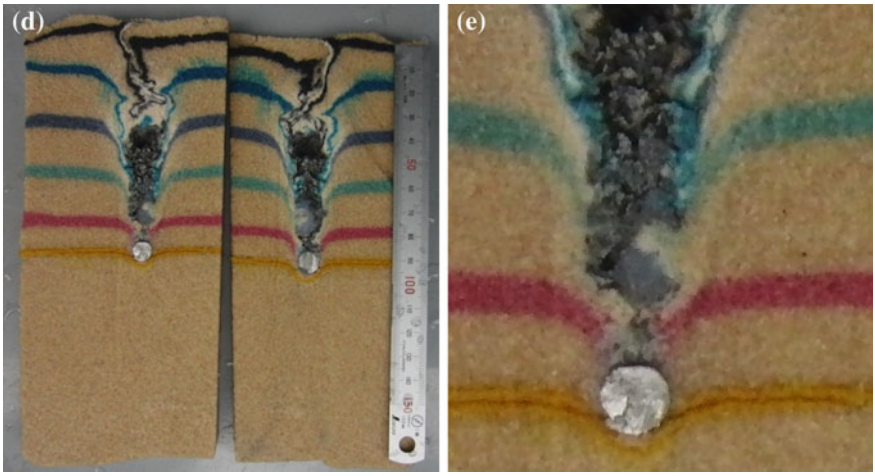

Fig. 11.28 (continued)

from the bottom. The sphere moved at high-speed and penetrated colored layers symmetrically toward the bottom forming a cavity. The internal cavity wall is covered with white sand grains. The white powders were created by the cracked sand grains due to the contact with the high-speed sphere or the exposure of the high pressures behind the bow shock wave. The luminous emission was created due to the fracture of the sand grains. The shape of the cavity resembled the shape of a wake flow but the wall was covered with carbon soot. The carbon soot was created by the thermal decomposition of polycarbonate sabot which followed the sphere as observed in Fig. 11.27b–d. The sphere's trajectory was straight so that the deformation of the color layers resembled the velocity profile in boundary layers.

A strong earthquake attacked the laboratory on March 11, 2013 and damaged the facility for conducting the sand impact experiment. Immediately after this incident, the recovered started. The image shown in Fig. 11.28d was the results of the experiment collected after the incidence and the author's final experiment taken on March 29th, 2013 just before his retirement on March 31st, 2013.

At the moment of the projectile impact on the sand layer, a splash of sand grains covered the entire open space and then the impact crater was covered by a falling fresh sand grains. The pattern of color layer's deformation became asymmetrically even though the experimental arrangement was symmetrical. The asymmetrical sedimentation would be attributable to the shape of the test section of 33 mm 100 mm. Figure 11.28d shows the result of the impact of a 9.5 mm diameter sphere at the impact speed of 1.01 km/s. The whole piece of the sabot impacted following the sphere and thermally decomposed inside the cavity created by the sphere. Hence the cavity was totally blackened by carbon soot. The deviation of the deformed color layers from their original horizontal positions would explain the history of deceleration of the sphere speed.

11.4 Shock Waves in Volcanic Eruptions

Volcanic eruptions occur, when the energies deposited in magma are released suddenly and the magma fragmentations take place. Then volcanic eruptions are more or less linked with shock wave phenomena (Glass 1975). Then volcanic eruptions would be reviewed from the point of view of the shock wave research. Analogue experiments of shock wave generations during explosive eruptions and the resulting shock wave propagation in air are readily investigated in shock tubes. However, shock tube experiments are limited only in the laboratory scale. Appropriate numerical simulations would be only a possible approach to reproduced volcanic eruptions. Volcanic eruptions are reviewed from the shock wave research (Takayama and Saito 2004).

11.4.1 In Situ Observation of Eruption

A project started to measure shock wave over-pressures in situ when Mt. Aso, Nakadake erupts. A pressure transducer by using a PVDF (poly vinyl denefluoride) piezo film was manufactured in house and was calibrated by comparing its output signal with that obtained by Kistler pressure transducer model 603B. The pressure transducer was installed at the edge of a stainless steel bar and was positioned in a bunker located on the top of the cliff overlooking a caldera of Mt. Aso Nakadake. Output pressure signals were then converted to optical signals, transmitted to the Aso Volcano Museum located 4 km away from the volcanic mouth, and stored in a digital memory placed in the Museum. The data stored in the digital memory were updated via the telephone line from the Institute of Fluid Science in Sendai. Figure 11.29 is an illustration of the data acquisition and their transmission from the volcano to the Museum. With this arrangement, the time variation of the pressure released from the volcanic conduit would be monitored in Sendai.

Figure 11.30 show the installation of a pressure transducer in 1995 inside the bunker, which was constructed at the top of the cliff overlooking the caldera of Mt. Aso, Nakadake. It was anticipated at that time that the eruption would occur shortly but Mt. Aso was quiet until the project was cancelled in 2013. When a progress report of this project was presented in a conference, a volcanologist commented that it would be a nice effort to study the eruption by installing such an equipment on the Mt. Aso. Cynically, when this project was cancelled, Mt. Aso erupted violently.

11.4.2 Numerical Simulation

At the same time, a super-computation was conducted to simulate numerically over-pressures and to compare the numerical result with the measured ones if Mt.

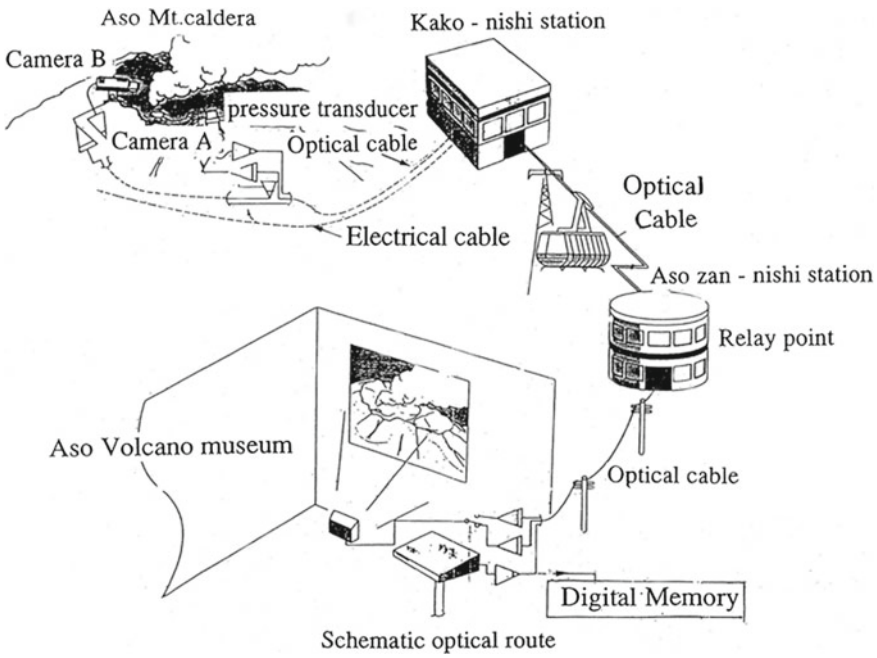

Fig. 11.29 The installation of a pressure transducer at the volcanic mouth of Mt. Aso. The signal is transmitted to the Aso Volcano Museum located 4 km away from the Mt. Aso (Takayama and Saito 2004)

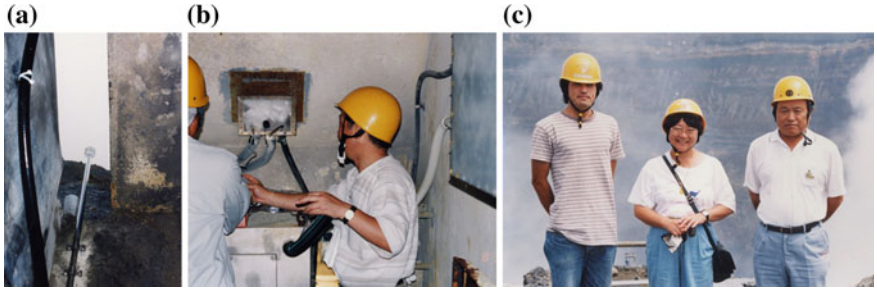

Fig. 11.30 The in situ pressure measurement of Mt. Aso in 1995; **a** A pressure transducer looking down a caldera of Mt. Aso; **b**, **c** installation of a pressure transducer in a bunker

Aso, Nakadake may erupt any time. Figure 11.31a shows a three-dimensional computational mesh describing Mt. Aso, Nakadake. The mesh was constructed by referring the digital map published by the former Geographical Survey Institute, presently the Geospatial Information Authority of Japan. In Fig. 11.31a, the position of the volcanic mouth was shown by a red arrow and the position of the pressure transducer was installed was shown by a blue arrow. Figure 11.31b–d

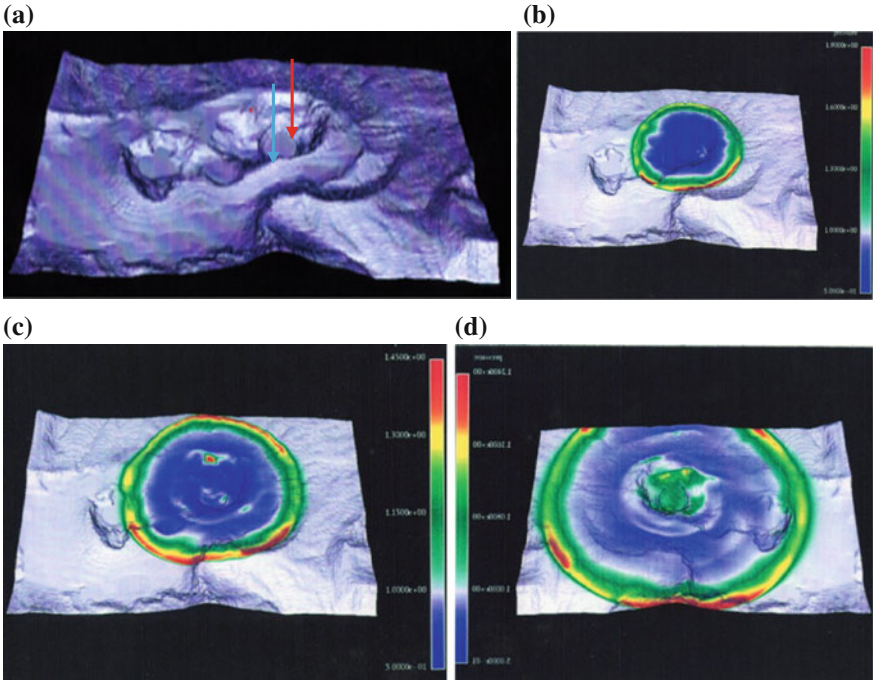

Fig. 11.31 The numerical pressure distributions behind a blast wave expected to occur at Mt. Aso eruption: **a** three-dimensional meshes from digital topological map; **b** 0.62 s; **c** 0.95 s; **d** 1.73 s

show temporal pressure distributions simulated by the late Professor Voinovich of the Ioffe Institute, Academy of Science Russia (Voinovich et al. 1999). The simulations were conducted. Different initial conditions were assumed in the volcanic conduit which was a vertical shaft filled with high temperatures and high pressures mixtures of air and foreign gases. Numerical scheme was the three-dimensional Euler solver on unstructured meshes which was flexible enough to accurately express the complex ground geometry. The initial conditions were tuned to match with the pressure history measured at the position as shown with a blue arrow in Fig. 11.31a. In Fig. 11.31b–d, the shock wave propagated along complex geometry and reflected locally from three-dimensional boundaries. These complex geometries significantly contributed to shock wave attenuation. In Fig. 11.31d the shock wave already passed the point at which the pressure transducer was installed.

11.4.3 Water Vapor Explosion

A water vapor explosion is one of the mechanisms which trigger volcanic eruptions. An analogue experiment was carried out for understanding the procedure of

interactions between a melted metal droplet and gas bubbles. Observations were conducted to confirm whether or not molted tin droplets falling into water would shatter. It often happened in steel industry that if a large volume of melted metal dropped into water, the contact between the melted metal explosively vaporize water. This is the so-called water vapor explosion and is closely linked with a magma water vapor explosion which would trigger the eruption.

Figure 11.32a–c show single exposure interferograms of melted tin droplets falling in water. The droplet was exposed to underwater shock wave generated by the explosion of a 10 mg AgN_3 pellet. Figure 11.32c shows the generation of reflected shock waves and wavelets from bubble surfaces but successive explosion was not observed (Kitamura 1995). There is a so-called a critical mass of the melted tin below which the successive disintegration never happens to occur. The experiment was initiated firstly to determined the critical mass. At first, the critical mass is believed to be based on the parameters; mass of melted tine; over-pressure of shock waves; and the bubble size. It was expected that through these parametric study, the critical mass of melted tin could be estimated. However, it was not possible to estimate the critical mass simply by assuming these parameters. The visualization presented here is a preliminary parametric study for determining the critical mass.

11.4.4 Magma Fragmentation

An analogue experiment of the shattering of fragmented debris particles was conducted in the 60 mm × 150 mm diaphragm-less vertical shock tube. Figure 11.33a shows the vertical shock tube designed for conducting an analogue experiment in which the dynamics of magma fragmentation is visualized. This shock tube was designed to conduct dusty gas shock tube experiment having a relatively large cross section. A high pressure chamber had a diaphragm-less structure, in which a quickly moving piston served as a diaphragm opening. The high pressure chamber was placed horizontally on the first floor. The vertical low pressure channel had a 60 mm 150 mm cross section and 6000 mm in length and connected to acrylic observation windows having 150 mm × 1700 mm field of view. Polystyrene beads having density 20 kg/m^3 and diameter of 4.0 ± 0.2 mm, Styrocell M551X, product of Shell International Petroleum Company were filled in the test section. In order to trace the motion of beads, some of the beads were dyed various colors. The experiment was conducted for Ms = 1.36 in atmospheric air and at room temperature. Figure 11.33b show the sequential observation of shock wave loading on a polyethylene bead layer. The test section was illuminate with a flood light and the observation was conducted with high-speed video camera Shimadzu SH100 at the framing rate of 10^5 frame/s. Upon the shock wave loading, the polyethylene bead layers were compressed. Soon the beads on the surface were lifted up into air driven by the shock wave reflected from the bottom wall. The bead motion would be analogous to the magma fragmentation in the volcanic conduits (Kitagawa et al. 2006).

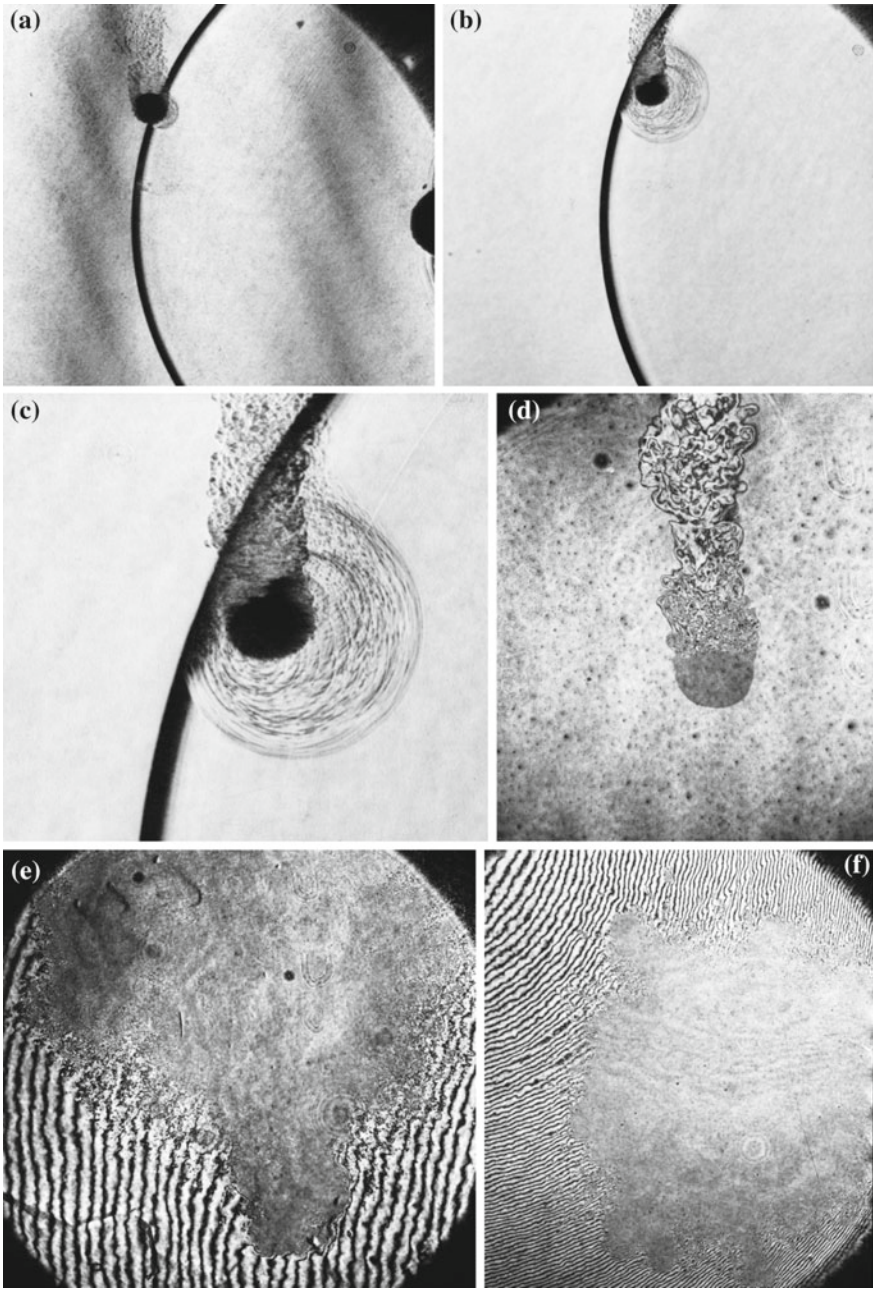

Fig. 11.32 Analogue experiments of water vapor explosion of a melted tin droplet falling into water. A Shock wave was generated by exploding a 10 mg AgN_3 pellet: **a** #94010409; **b** #94010501; **c** enlargement of (**b**); **d** #93101105; e #93093001; **f** #93093005 (Kitamura 1995)

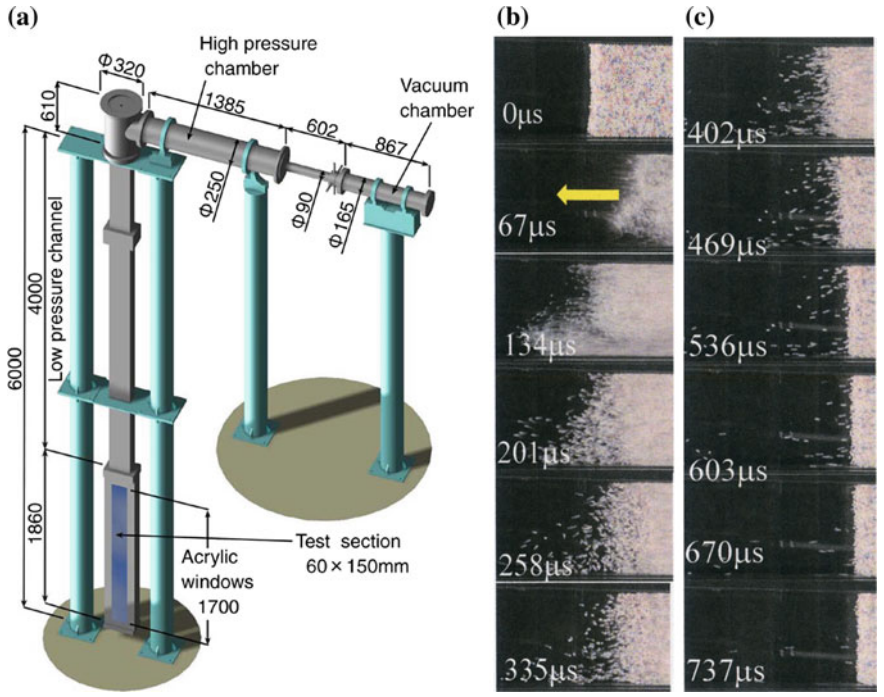

Fig. 11.33 A 60 mm × 150 mm diaphragm-less vertical shock tube: **a** vertical shock tube; **b**, **c** sequential observation of polyethylene beams exposed to a shock wave for Ms = 1.36

In Fig. 11.34a, three pressure transducers, Kistler Model 603B, were distributed along the vertical test section and a transducer was placed at the end wall. In Fig. 11.34b, the pressure histories from these transducers are presented for Ms = 1.36. The pressure history from the first #1 transducer shows sharp pressure rises corresponding to the incident and reflected shock waves but the pressure behind the incident shock wave is followed by an expansion wave due to the short high pressure chamber. However, the arrival of the expansion wave promoted the shattering of the beads. The signal out of the second #2 transducer shows the pressure enhancement only at the earlier stage and then a continuous decrease due to the shattering of the polyethylene beads toward the upstream. These pressure histories agree well with the results of observation seen in Fig. 11.34b.

It is concluded that the wave motion occurring in a high pressure chamber is similar to the wave motion and also the movement of debris in a volcanic conduit. However, during the eruptions, the reflected expansion wave from the opening of the volcanic mouth not only promotes the process of degassing in magma but also accelerating the fragmentation of a lave layer located at the bottom of the volcanic conduit. An analogue experiment of the fragmentation of a lava layer was conducted in a vertical shock tube (Yamamoto et al. 2008).

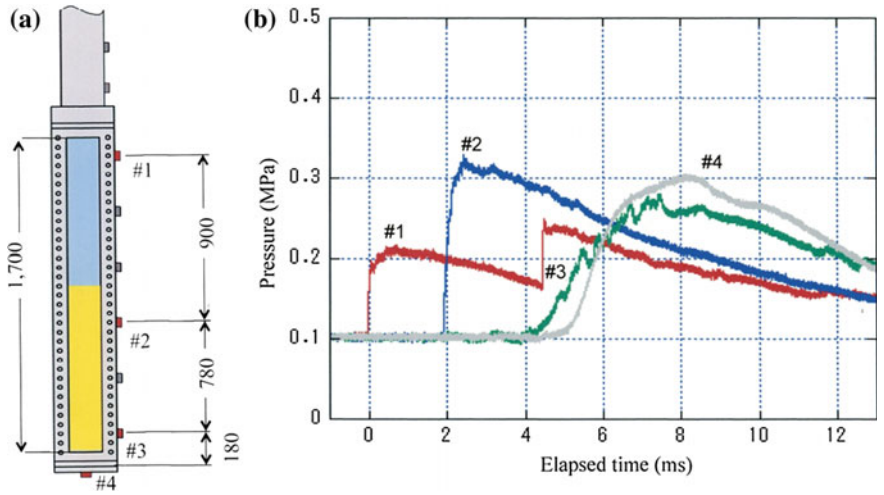

Fig. 11.34 Vertical shock tube test section: **a** pressure transducer distribution; **b** pressure recording

11.5 Shock Wave Interaction with Letters SWRC

The shock wave interaction with letters SWRC which stand for Shock Wave Research Center was sequentially visualized by double exposure holographic interferometry for Ms = 1.20 in atmospheric air at 294.0 K. Capital letters of SWRC of 60 mm in thickness made of carbon steel were arrayed in the test section of the 60 mm × 150 mm diaphragm-less shock tube and the result of sequential interferograms were edited in an animated display (Abe 1989) in Fig. 11.35. Interaction with curved boundaries, reflections and focusing from concave walls, and diffraction at corners of shock waves created very interesting wave patterns. At the same time, it would be nice if these patterns are reproduced numerically.

11.6 Shock Waves Generated in Daily Life

There are many phenomena in our daily life that create shock waves and their characters are very analogous to the shock wave phenomena. Although many of them miss mathematical formulations, the phenomena indeed have analogous characters to shock wave and then are called shock wave-like phenomena. The propagation of rumors, the transmission of information, panic motion in human cloud, and traffic flows are typical shock wave like phenomena.

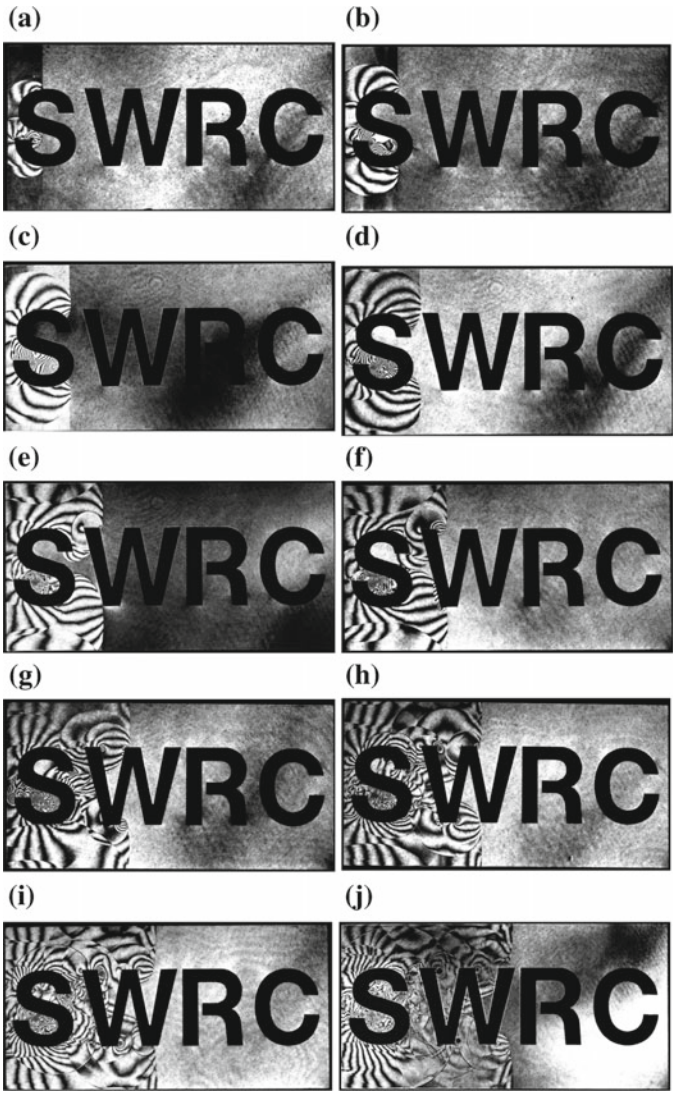

Fig. 11.35 Shock wave propagation along letters SWRC at Ms = 1.20 in atmospheric air at 294.0 K: **a** #97112103, 240 μs from trigger point, Ms = 1.195; **b** #97112112, 270 μs, Ms = 1.208; **c** #97112115, 300 μs, Ms = 1.197; **d** #97112118 320 μs, Ms = 1.200; **e** #97112130, 360 μs, Ms = 1.205; **f** #97112505, 390 μs, Ms = 1.201; **g** #97112510, 420 μs, Ms = 1.200; **h** #97112513, 460 μs, Ms = 1.202; **i** #97112518, 490 μs, Ms = 1.201; **j** #97112522, 530 μs, Ms = 1.209; **k** #97112527, 580 μs, Ms = 1.204; **l** #97112533, 600 μs, Ms = 1.201; **m** #97112615, 700 μs, Ms = 1.198; **n** #97112618, 730 μs, Ms = 1.20; **o** #97112705, 770 μs, Ms = 1.205; **p** #97112710, 820 μs, Ms = 1.204; **q** #97112713, 850 μs, Ms = 1.202; **r** #97112719, 900 μs, Ms = 1.204; **s** #97112722, 930 μs, Ms = 1.204; **t** #97112726, 970 μs, Ms = 1.198; **u** #97112734, 1030 μs, Ms = 1.198; **v** #97112736, 1050 μs, Ms = 1.206

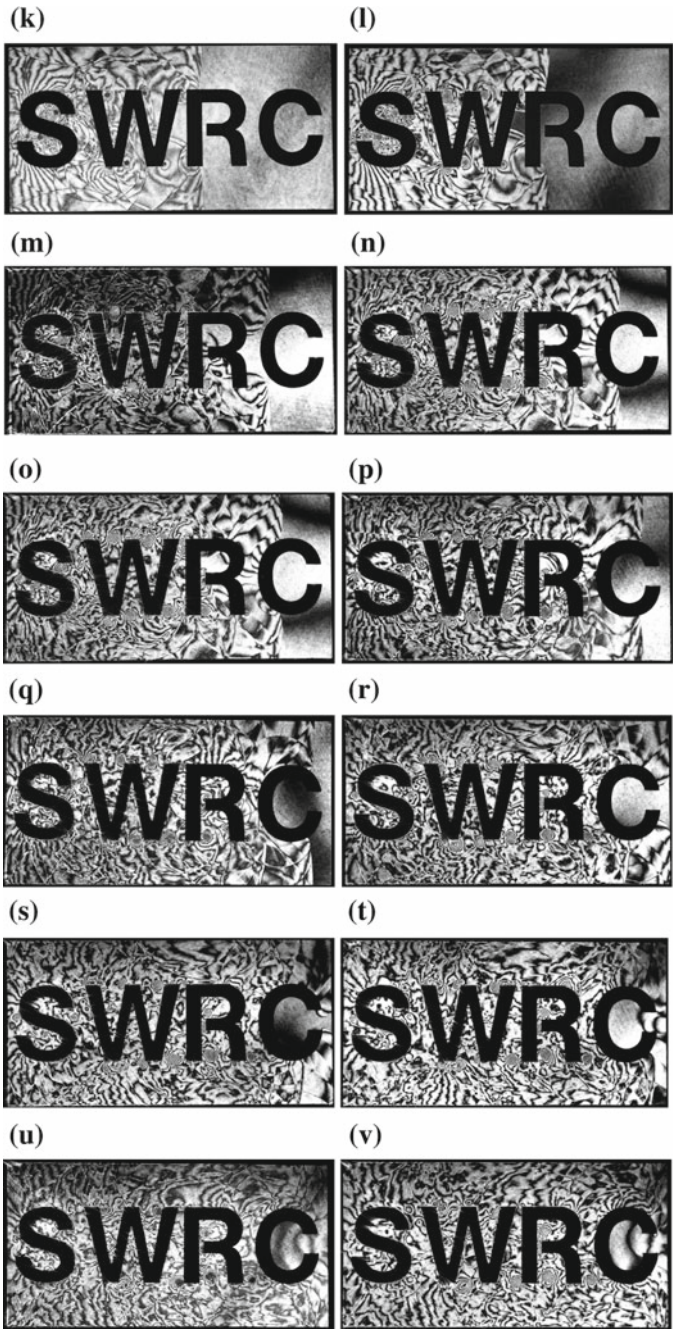

Fig. 11.35 (continued)

11.6.1 Swing of a Whip

Glass commented in his book (Glass 1975) that the swing of a whip generated a cracking noise which was similar to a shock wave. The cracking noise was visualized by using a pair of 1000 mm diameter schlieren mirrors and was recorded with high-speed digital camera Shimadzu SH100. The light source was a conventional flash lamp. In swinging a whip, its tuft eventually moved at supersonic speed driving a shock wave. Figure 11.36 sequentially show the shock wave formation during the swing of a whip. The tuft moved at approximately 450 m/s and the resulting shock Mach number Ms was about 1.30 in atmospheric air. If a planar shock wave is assumed, the over-pressure of the shock wave of Ms = 1.36 would be 180 kPa, which is destructive enough to damage targets.

11.6.2 Blow of Trobone

Some composers of symphonies, for example, Mahler favored trombone blown in *fff*. Considering the structure of the trombone, it can generate a startlingly intense

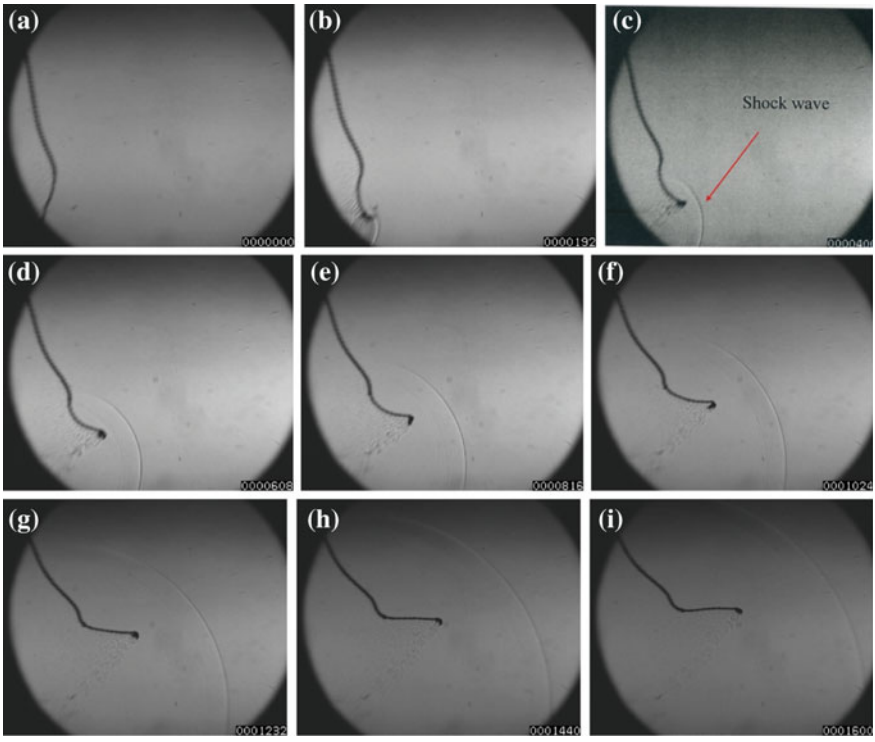

Fig. 11.36 A shock wave created at the tuft of a whip recorded by Shimadzu SP100 at 10^6 frames/s

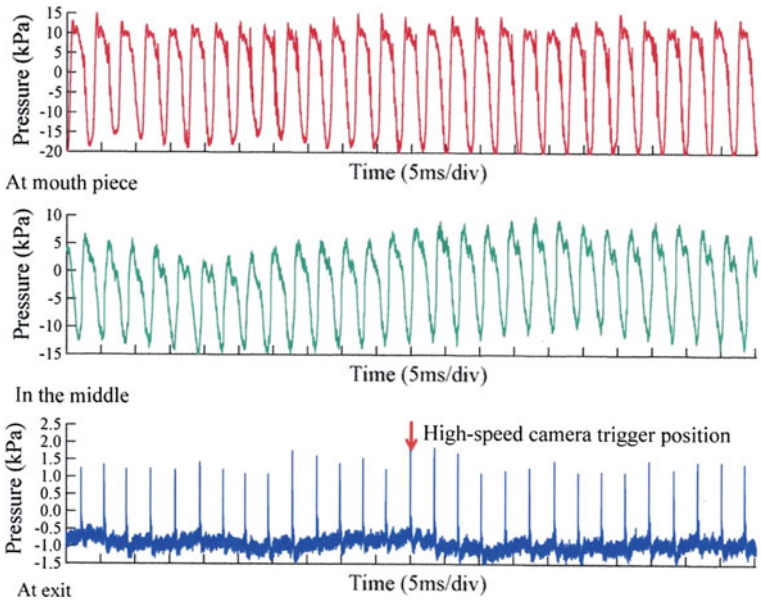

Fig. 11.37 Comparison of pressure profiles at trombone blow measured at three position: at mouth piece, in the middle position and at the exit

sound, in other words, a compression wave having a profile very close to that of a weak shock wave. It is described in a book of Physics of Musical Instruments (Fletcher et al. 1998) that players may have their physical risk when they try to produce strong sounds in blowing a trombone. Nevertheless, a trombone blow can generate weak shock waves. The sound pressures generated by a trombone blow was measured by pressure transducers, Kistler 603B placed at the mouth piece, the center of the tube length; and at the exit. Figure 11.37 shows variations of pressure measured at these positions. The ordinates denote pressures in MPa and the abscissae denote elapsed time in 5 ms in division. Measured peak pressures reach to about 10 kPa, which means strong breaths are blown into the mouth piece. The pressures so far blown into the tube attenuate quickly but the wave heads are steepened when waves reached peak pressures of about 5 kPa in the middle position. At the exit, the pressure profile is so steepened forming a weak shock wave having the peak pressure of 1.5 kPa. This over-pressure corresponds to a shock wave of Ms = 1.009. The trombone player in this experiment was a member of a university student orchestra.

The resulting weak shock waves were visualized by interferogram and direct shadowgraph recorded by the high speed video camera Shimadzu SH100 at the framing rate of 10^6 frame/s. Figure 11.38 show double exposure interferograms. Slightly dark shadow seen in Fig. 11.38a shows a weak shock wave of Ms = 1.009. Figure 11.38a show a stand holding a pressure transducer facing to the exit of the trombone and a shock wave. Figure 11.38b was taken at 300 μs after the

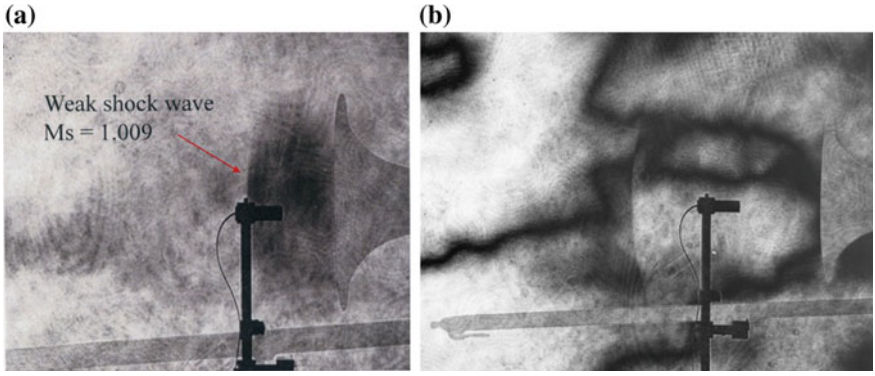

Fig. 11.38 Double exposure holographic observation of compression waves released from a trombone: **a** #10091612; **b** #10091609

observation in Fig. 11.38a. A weak shock wave is shown as a discontinuous change in the grey contrast. Such a weak shock wave was observed in a grey shadow released from the exit of the train tunnel simulator.

Figure 11.39 show sequential direct shadowgraphs of the transmission of a weak shock wave released from a trombone.

11.6.3 Visualization of Flows Around an Arrow of Japanese Archery

The Japanese archery was one of the traditional marshal arts inherited from old time. Today it is a popular sport. The length of arrows is close to 900 mm so that the visualization of the whole length of the arrows in free flight requires 1000 mm diameter schlieren mirrors. The speed of arrows in free flight is about 50 m/s but is too slow to exhibit any effects of compressibility. In order to create an effect of compressibility, it was decided to decrease its surface temperature down to nitrogen temperature.

Professor Sato of Tohoku University, a master of Japanese archery, was invited to shoot arrows. He shot an arrows so as to fly it across 1000 mm diameter schlieren mirrors. Figure 11.40a shows his bowing in front of the schlieren mirror. Figure 11.40b shows an experimental arrangement of measuring the arrow speed by a time of flight method.

In order to create the density gradient over an arrow, it was immersed in liquid nitrogen contained in a Dewar for 5 min. As soon as the arrow's surface temperature became close to the liquid nitrogen temperature, it was taken out of the Dewar. Professor Sato shot it within 20 s as seen in Fig. 11.40a. Figure 11.41 shows the temperature variation on the arrow surfaces monitored by using

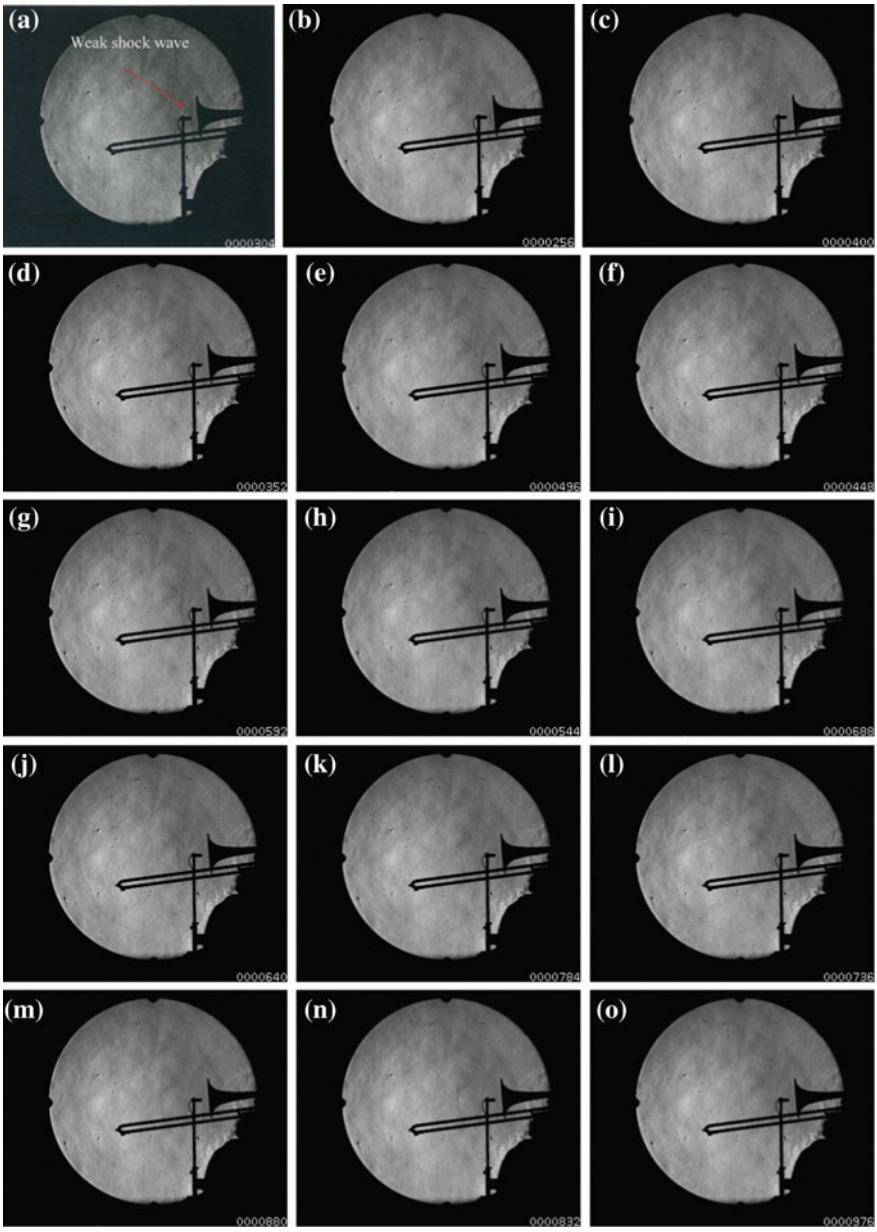

Fig. 11.39 The sequential observation of weak shock waves released from at a trombone

thermocouples at the arrow head, position A and at 200 mm from the arrow head, position B. The ordinate denotes the surface temperature in K. The ordinate denotes elapsed time in s.

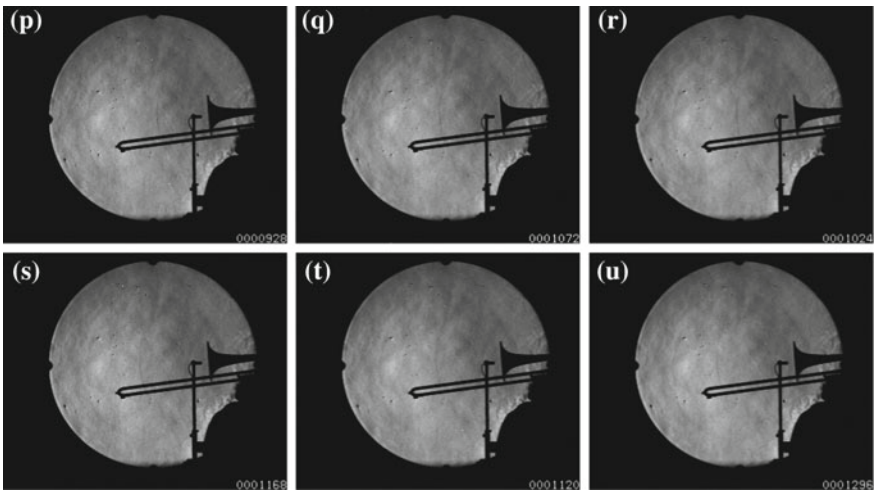

Fig. 11.39 (continued)

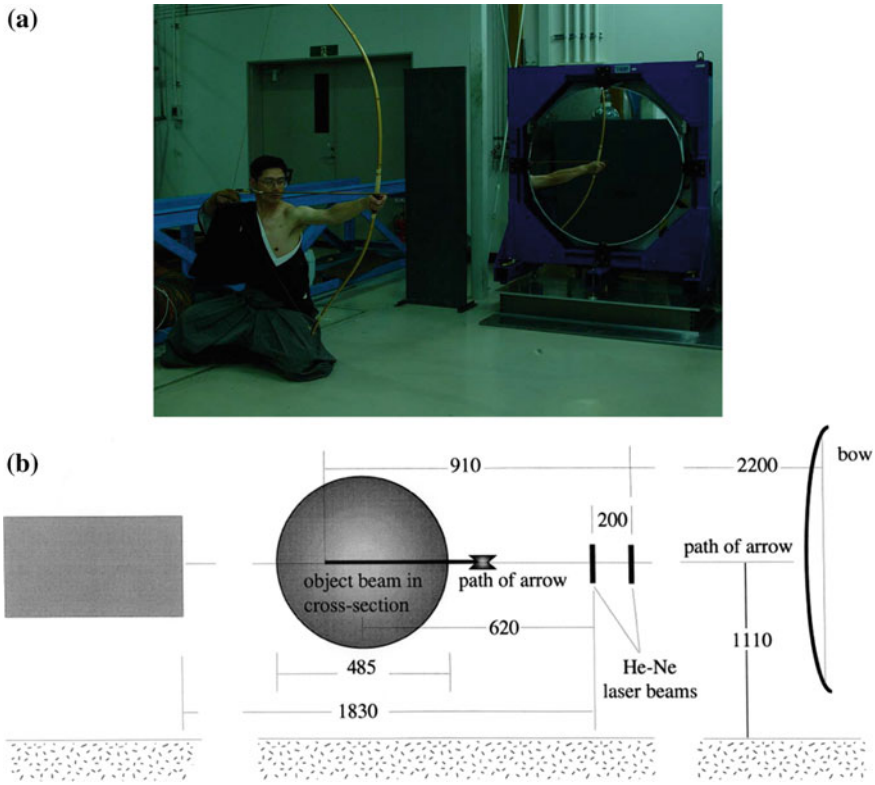

Fig. 11.40 The visualization of an arrow of Japanese archery: **a** professor Sato's shooting an arrow in front of a 1000 mm diameter schlieren mirror; **b** arrangement of measuring the arrow speed (Sato and Takayama 1999)

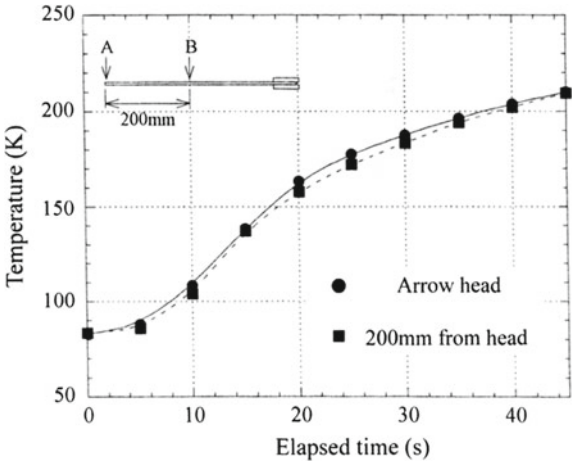

Fig. 11.41 Time variation of surface temperature on the arrow

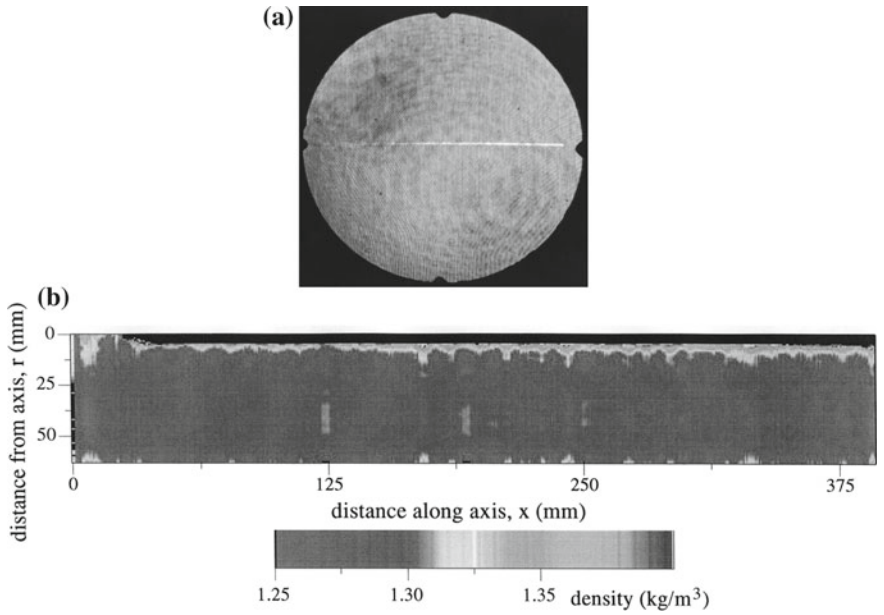

Fig. 11.42 Temperature gradient along an arrow: **a** #02070507; **b** density profile

When taking it out of the Dewar, the temperature increased almost identically at the positions A and B. When the surface temperature recovered to be about 160 K after 20 s. The temperature gradient across the thermal boundary layer developing along the arrow in free flight would be a good maker to demonstrate the variation of

the density gradient across the boundary layer in the infinite fringe interferometry. Figure 11.42 shows the flight of an arrow at the speed of 50 m/s. It should be noticed the entire length of the arrow was visualized for the first time. Applying the Fourier fringe analysis to the fringe distribution seen in Fig. 11.42, the density and temperature distributions over the arrow were determined (Houwing et al. 2005). Assuming a laminar boundary layer and the Prantdl number Pr = 1, the velocity profile is readily obtained from the temperature profile. Figure 11.40b shows the density profile. The present research was a preliminary work demonstrating the capability of holographic interferometry to incompressible flow study.

11.7 Mass Extinction

In the history of the earth, every 25.6 million years on average, giant asteroids impacted on the earth. The frequent impacts, in a geological time scale, were enough to discontinuously change chronological periods of the earth and decisively affected the course of the evolution of creatures on the earth (Hosseini et al. 2016). A devastating mass extinction of species took place in about 65 million years ago. Geological survey revealed that the asteroid with an estimated diameter over 10 km obliquely entered into the earth atmosphere and impacted on the Yucatan Peninsula creating a 170 km diameter crater (Rampino 1999).

Underwater shock waves and seismic waves contributed to mass extinction. Marine creatures having lungs and balloons were killed spontaneously by the exposure of underwater shock waves but ocean bottom dwellers such as foraminifera survived. Then it was hypothesized that underwater shock waves only locally contributed to the mass extinction.

Ocean bottom dwellers, ostracodas, about 50 μg in weight and 0.4 mm × 0.4 mm in size were sampled from the silt layer of the Matsushima Bay near Sendai. The sampled ostracodas were kept in the original sea water in the refrigerator for a while. These were micro-creatures representing ocean bottom dwellers.

Figure 11.43a shows a 500 mm × 500 mm × 500 mm stainless steel test chamber equipped with a needle hydrophone and a support detonating a 100 mg PETN pellet. Containers made of polyamide accommodating ostracodas were placed on the bottom of the test chamber. Figure 11.44b shows the polyamide container of 30 mm in diameter and 10 mm in thickness having 5 pits of 3 mm in diameter and 1.5 mm in depth. Five ostracodas were placed in each pit. The container was covered with a thin latex rubber membrane disconnecting the pit from the test environment. The experimental procedure is described in Hosseini et al. (2016).

Figure 11.44a shows time variation of over-pressures generated by explosion of 100 mg PETN pellets. The over-pressures were measured at the stand-off distance 60 and 120 mm using a 0.5 mm diameter PVDF needle hydrophone (Mueller Ingeniertechnik). The loading pressures were controlled by varying the stand-off distance between the center of the explosion and the ostracoda containers. Figure 11.44b shows the results. The ordinate denotes number of ostracodas survived

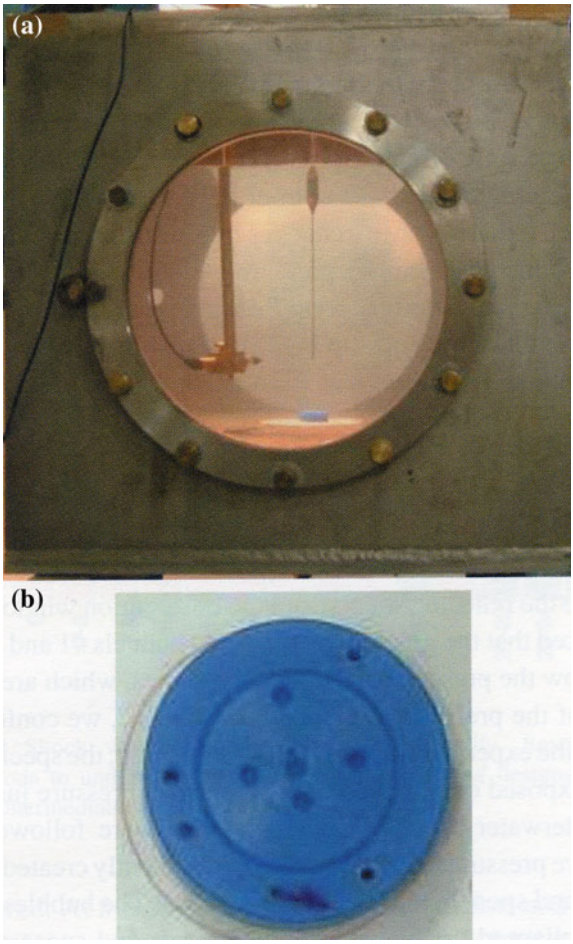

Fig. 11.43 Experimental arrangement: **a** test chamber; **b** ostracoda placed inside each test samples

or dead. The abscissa denotes the over-pressures in MPa. Red color denotes survivors in a week after the shock exposure, blue denotes survivors only for a first week and dead afterward, black denotes spontaneous dead. 13 samples at 0 MPa are alive as reference without shock wave exposures. The number of survivors decreases with increase in the over-pressures. At the over-pressure ranging from 12 to 15 MPa, the number of survivors decreases and at over 17 MP almost all ostracodas dead. The results indicated that upon the direct exposure of underwater shock waves having over-pressures exceeding 17 MPa, the ostracodas were killed.

The ocean bottom layers are composed of sediments of marine snow and layers of silt in which osracodas and foraminiferas live. The silt layer would effectively mitigate shock waves while their propagation. In the silt layer. Hence the ocean bottom dwellers living inside the shallow silt layer would survive against much stronger underwater shock wave exposure. In conclusion, the present analogue experiment verified the survival of the ocean bottom dwellers against the asteroid impact.

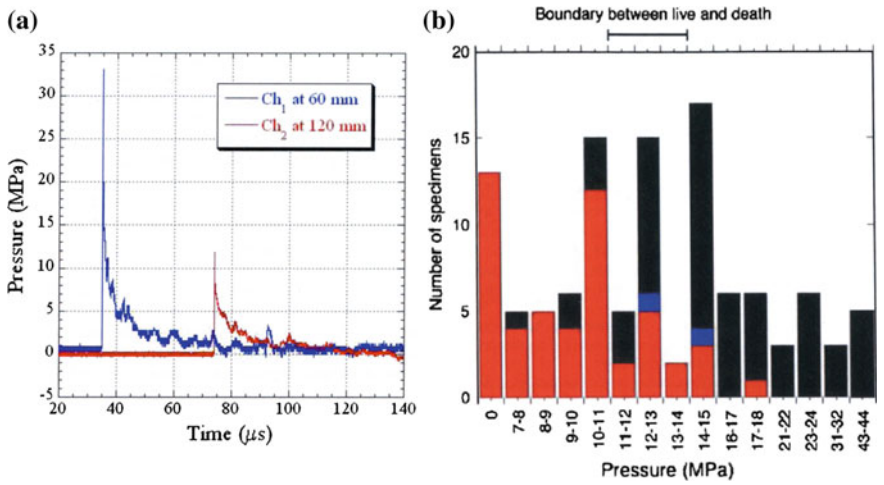

Fig. 11.44 Results: **a** pressure history at stand-off distances of 60 and 120 mm; **b** mortality

11.8 A Water Wave: Shock Wave-like Phenomenon

The motion of a sea wave approaching toward a shore has its inherent speed of transmitting the wave motion that is proportional to a square root of the water depth. This is equivalent to a sound speed in media and defined in Courant and Friedrichs (1948). When a wave is propagating at a constant speed toward the shore the depth of which becomes gradually shallower, the equivalent sound speed becomes gradually slower. Hence, the ratio of the propagation speed of water wave to the equivalent sound speed exceeds unity. Physically, in applying gas-dynamic analogy to the motion of a water wave, the water wave changes its character from a subsonic flow to a supersonic flow when the water wave speed became supersonic. In a supersonic water wave, its shape is gradually steepened. The wave motion and its shape were equivalent to the formation of a shock wave phenomenon in gas-dynamic. The appearance of a dispersed but discontinuous wave front moving over shallow shores is an analogous phenomenon to a shock wave in gas dynamics: the so-called shock wave-like phenomena (Courant and Friedrichs 1948; Glass 1975; Takayama et al. 1994). There are many shock wave-like phenomena in our daily life. However, the most of the shock wave-like phenomena have no mathematical models. On the contrary in the case of water waves, the mass continuity across water waves and the motion of water waves were mathematically expressed in the form of conservation equations as following:

$$\partial \mathrm{E}/\partial \mathrm{t} + \partial \mathrm{F}/\partial \mathrm{x} + \partial \mathrm{G}/\partial \mathrm{y} = 0$$

where t, u, v are time and velocity components in the x, y direction: $\phi = \mathrm{gH}$; g and H are the gravitational constant, and the depth of a water wave, respectively:

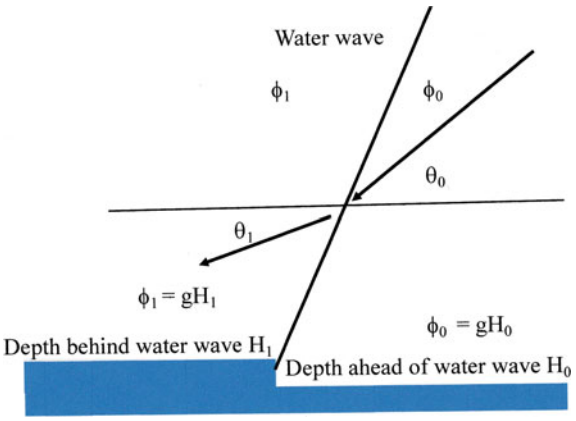

Fig. 11.45 Conditions across an oblique water wave

$E = (\phi, \phi u, \phi v)$, $F = (\phi u, \phi u^2 + \phi^2/2, \phi uv)$, $G = (\phi v, \phi uv, \phi v^2 + \phi^2/2)$. These partial differential equations are valid in the wave motions over shallow water and are equivalent to a special case of the gas-dynamics conservation equations having the specific heats ratio of $\gamma = 2$. Due to this analogy, shallow water tables were once used as replacements of supersonic wind tunnels in a working gas having the specific heats ratio of $\gamma = 2$. However, it should be noticed that the energy conservation is not taken into consideration in this formulation.

Figure 11.45 schematically describes an oblique water wave propagating from the right to the left at its inclination angle of θ_0 and deflected by θ_1. Across the oblique water wave, the water depth changes from H_0 to H_1.

The relationship of the continuity and the equation of motion across an oblique water wave are analogous to the Rankin-Hugoniot equations in gas-dynamics: Equations of continuity are given by

$$\phi_0 u_0 \sin\theta_0 = \phi_1 u_1 \sin(\theta_0 - \theta_1) \tag{11.1}$$

and

$$u_1 \cos\theta_0 = u_1 \cos(\theta_0 - \theta_1); \tag{11.2}$$

the equation of motion is given by

$$\phi_0 u_0^2 \sin^2\theta_0 + \phi_0^2/2 = \phi_1 u_1^2 \sin^2(\theta_0 - \theta_1) + \phi_1^2/2. \tag{11.3}$$

Then the jump of a water wave, H_1/H_0, is readily determined by solving abovementioned equations:

$$\begin{aligned} H_1/H_0 &= \{(1 + 8\mathrm{Fr}\sin^2\theta_0)^{1/2} - 1\}/2 \\ &= \tan\theta_0/\tan(\theta_0 - \theta_1), \end{aligned} \tag{11.4}$$

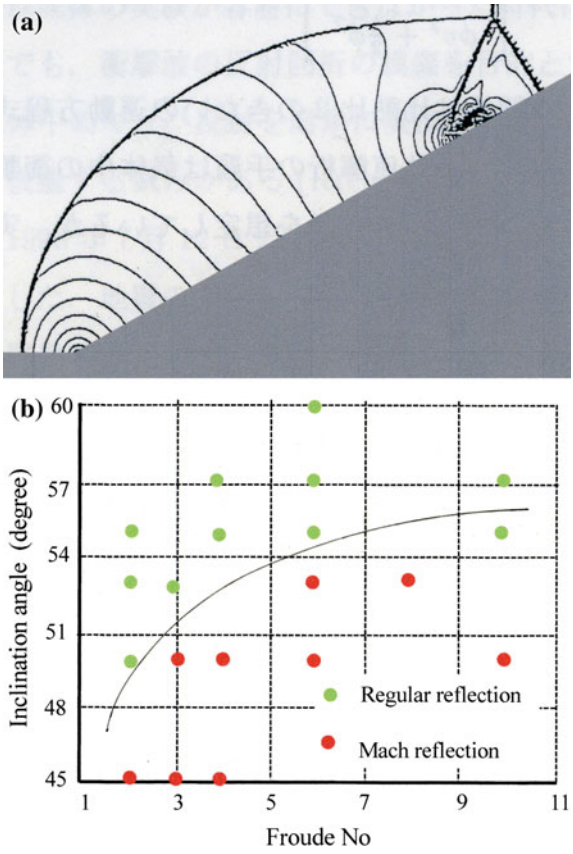

Fig. 11.46 Numerical simulation of water wave reflection: **a** typical Mach reflection pattern over wedge of 30° for Fr = 9.0; **b** the domain and boundary of reflected shock waves

where Fr is called as the Froude number defined as $Fr = u_0^2/\phi_0$. The Fr governs the dynamics of the water wave and is equivalent to Mach number in gas-dynamic shock waves. The Fr becomes larger for higher water wave speed or the shallower the wave depth.

Figure 11.46a shows contour lines of wave heights reflected over a 60° inclined water wave for Fr = 9. Each line shows a line of equal height and is obtained by solving the above mentioned conservation equations. This display was adjusted to match with the gas dynamic shock wave reflection from a wedge of wedge angle 30°. The obtained reflection pattern is similar to a Mach reflection. Wave heights become highest at the triple point and along the Mach stem.

The conservation equations were solved numerically for selective combinations of the Fr number and the inclination angles. The obtained reflected wave patterns were either a Mach reflection or a regular reflection in gas-dynamic shock waves. Figure 11.46b summarizes computational results. The results were displayed to match with the gas-dynamic shock wave reflections from wedges. The ordinate denotes the wedge angle in degree, that is, $90° - \theta_0$. The abscissa denotes the Fr

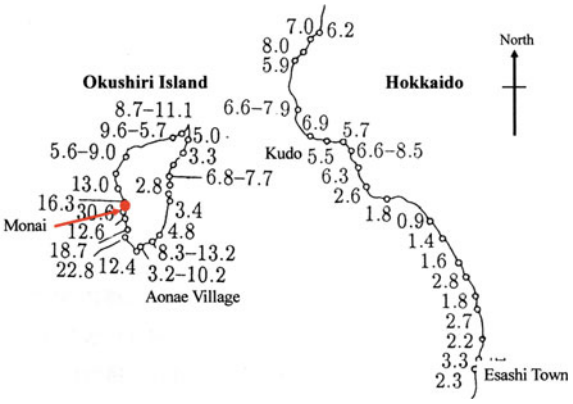

Fig. 11.47 The height of a Tsunami when it attacked the Okushiri Island on July 12th, 1993. Notice that the Monai beach uniquely recorded a wave height over 30 m

which is equivalence to Ms. Red filled circles denote Mach reflection, MR. Green filled circles denote regular reflection, RR. From the observation of these reflection patterns, a detachment criterion was empirically estimated. Mach reflection patterns were clearly identified as seen in Fig. 11.46a but regular reflection patterns were so smeared that they are not necessarily clearly identified. Reflected water waves merge at a localized point and result in focusing of water wave, in which the height of the water wave becomes locally very high. The focusing of the water wave was observed in nature when the tsunami attacked the shore.

At 7:30 p.m., on July 12th, 1993, an earthquake in the Richter scale 7.5 occurred at the western offshore near the Okushiri Island in Hokkaido, Japan. Immediately after the earthquake, a destructive tsunami attacked the west coast of the Okushiri Island. Figure 11.47 shows the Okushiri Island and its opposite shore on the western coast of Hokkaido. Small circles allocated along the coast shown in Fig. 11.47 were the location of the spots at which the wave heights were monitored. Along the eastern coast of the Okushiri Island, the higher second peak values of the wave heights indicated reflected waves from the western coast of Hokkaido. It should be noticed that the wave height at the Monai shore shown in a red filled circle on the coast of the Okushiri Island was singularly over 30 m. Taking the shape of the bottom of the coast in the neighborhood of the Monai shore into consideration, the appearance of such a wave height would be generated due to focusing of the water wave. The focusing of the tsunami would be numerically simulated, if the topographies of the bottom of the Monai coast are known.

References

Abe, A. (1989). *Study of diffraction of shock wave released from the open end of a shock tube* (Ph.D. thesis). Graduate School of Engineering, Faculty of Engineering Tohoku University.

Aratani, S. (1998). *Study of effects of shock waves on thin tempered glass manufacturing* (Ph.D. thesis). Graduate School of Engineering, Faculty of Engineering Tohoku University.

Courant, R., & Friedrichs, K. O. (1948). *Supersonic flows and shock waves*. New York: Wiley Inter-Science.

Fletcher, N. H., & Rossing, T. D. (1998). *The physics of musical instruments*. New York: Springer.

Glass, I. I. (1975). *Shock wave and man*. Canada: Toronto University Press.

Hashimoto, T. (2003). *Analytical and experimental study of hypersonic nozzle flows in free piston shock tunnel* (Doctoral thesis). Graduate School of engineering, Faculty of Engineering, Tohoku University.

Hosseini, S. H. R., Kaiho, K., & Takayama, K. (2016). Response of ocean bottom dwellers exposed to underwater shock waves. *Shock Waves, 26,* 69–73.

Houwing, A. F. P., Takayama, K., Jiang, Z., Sun, M., Yada, K., & Mitobe, H. (2005). Interferometric measurement of density in nonstationary shock wave reflection flow and comparison with CFD. *Shock Waves, 14,* 11–19.

Kitagawa, K., Takayama, K., & Yasuhara, M. (2006). Attenuation of shock waves propagating in polyurethane foams. *Shock Waves, 15,* 437–445.

Kitamura, T. (1995). *A study of water vapor explosion* (Master thesis). Graduate School of Engineering, Faculty of Engineering, Tohoku University.

Koremoto, K. (2000). *Experimental and analytical study of optimization of performances of a high enthalpy free piston shock tunnel* (Doctoral thesis). Graduate School of Engineering, Faculty of Engineering, Tohoku University.

Liepmann, H. W., & Roshko, A. (1960). *Element of gas-dynamics*. New York: Wiley.

Mark, H. (1956). *The interaction of a reflected shock wave with the boundary layer in a shock tube*. NACA TM 1418.

Matsumura, T., Inoue, O, Gottlieb, J. J., & Takayama, K. (1990). A numerical study of the performance of a two-stage light gas gun. *Report Institute of Fluid Science, Tohoku University, 1*, 121–133.

Nonaka, S. (2000). *Experimental and numerical study of hypersonic flows in ballistic range* (Ph.D. thesis). Graduate School of Engineering, Faculty of Engineering Tohoku University.

Numata, D. (2009). *Experimental study of hypervelocity impact phenomena at low temperature in a ballistic range* (Ph.D. thesis) Graduate School of Engineering, Faculty of Engineering Tohoku University.

Rampino, M. R. (1999). Evidence of periodic cosmic showers and mass extinction on earth. In Y. Miura (Ed.), *International Symposium on PIEC, Yamaguchi*.

Sato, A., & Takayama, K. (1999). Measurement of flight of an arrow, measurement and control. *Japan SoC, Automatic Control, 4*(4), 255–263.

Takayama, K., & Saito, T. (2004). Shock wave/geophysical and medical applications. *Annual Review Fluid Machine, 36,* 345–370.

Takayama, K., Miura, Y., Olim, M., Saito, T., & Toro, E. F. (1994). Mach reflection of water waves and the Okushiri Tsunami. In *Proceedings of the 1993 National Shock Wave Symposium* (pp. 487–490).

Voinovich, P., Timofeev, E. V., Saito, T., Takayama, K., Hyodo, Y., & Galyukv, A. O. (1999). An adoptive shock capturing method in real 3-D applications. In *Proceedings of the 2nd International Symposium on Shock Waves* (Vol. 1, pp. 641–646).

Yamamoto, H., Takayama, K., & Cooper, W. (2015). Evolution of luminous front at impact of a 1 km/s projectile into sand layers. In R. Bonazza & D. Ranjan (Eds.), *Shock Waves, Proceedings of the 29th ISSW, Madison* (Vol. 1, pp. 763–767).

Yamamoto, H., Takayama, K., & Kedrinskii, V. (2008). An analogue experiment of magma fragmentation behavior of rapidly decompressed starch syrup. *Shock Waves, 17*, 371–385.

Yang, J.-M. (1995). *Experimental and analytical study of behavior of weak shock waves* (Doctoral thesis). Graduate School of Tohoku University, Faculty of Engineering.